Title

Presynaptic NMDA receptors cooperate with local action potentials to implement activity-dependent GABA release from the reciprocal olfactory bulb granule cell spine

Authors

Vanessa Lage-Rupprecht[1,2], Li Zhou[1], Gaia Bianchini[1], S. Sara Aghvami[1,3,4], Max Mueller[1], Balázs Rózsa[5], Marco Sassoé-Pognetto[6] & Veronica Egger[1*]

Affiliations

1. Neurophysiology, Institute of Zoology, Universität Regensburg, 93040 Regensburg, Germany; 2. Department of Bioinformatics, Fraunhofer SCAI, 53757 Sankt Augustin, Germany; 3. School of Electrical and Computer Engineering, University of Tehran, 14395-515 Tehran, Iran; 4. School of Cognitive Sciences, Institute for Research in Fundamental Sciences (IPM), 19395-5746 Tehran, Iran; 5. Two-Photon Imaging Center, Institute of Experimental Medicine, Hungarian Academy of Sciences, 1039 Budapest, Hungary; 6. Neuroscience Department, University of Turin, I-10126 Torino, Italy.

Abstract

In the rodent olfactory bulb the smooth dendrites of the principal glutamatergic mitral cells (MCs) form reciprocal dendrodendritic synapses with large spines on GABAergic granule cells (GC), where unitary release of glutamate can trigger postsynaptic local activation of voltage-gated Na^+-channels (Na_vs), i.e. a spine spike. Can such single MC input evoke reciprocal release? We find that unitary-like activation via two-photon uncaging of glutamate causes GC spines to release GABA both synchronously and asynchronously onto MC dendrites. This release indeed requires activation of Na_vs and high-voltage-activated Ca^{2+}-channels (HVACCs), but also of NMDA receptors (NMDAR). Simulations show temporally overlapping HVACC- and NMDAR-mediated Ca^{2+}-currents during the spine spike, and ultrastructural data prove NMDAR presence within the GABAergic presynapse. This cooperative action of presynaptic NMDARs allows to implement synapse-specific, activity-dependent lateral inhibition and thus could provide an efficient solution to combinatorial percept synthesis in a sensory system with many receptor channels.

Introduction

Reciprocal dendrodendritic microcircuits can be found in several parts of the nervous system and are especially abundant in the vertebrate olfactory bulb (*Crespo et al. 2013*), where the dendrites of the principal mitral and tufted cells (MTCs) engage in such interactions with several major subtypes of local GABAergic neurons. In the glomerular layer, the MTC apical tuft is reciprocally connected to mostly periglomerular cell dendrites. In the external plexiform layer, the long MC lateral dendrites are densely covered with GABAergic synapses that mostly originate from reciprocal arrangements (*Bartel et al. 2015; Sailor et al. 2016; Matsuno et al. 2017*). While proximal circuits are thought to be mostly formed by granule cell (GC) spines (*Miyamichi et al. 2013*), there are also reciprocal dendrodendritic interactions with other GABAergic cell types such as SOM+ neurons, CRH+ neurons and most prominently parvalbumin/PV+ neurons that all feature aspiny, smooth dendrites (partially overlapping populations; *Toida et al. 1994; Lepousez et al. 2010; Huang et al. 2013; Kato et al. 2013; Miyamichi et al. 2013)*.

Thus the MC-GC synapse differs from the other bulbar reciprocal arrangements by its location within a large spine on the GC side. These spines feature particularly long necks (*Woolf et al. 1991*) which might serve to electrically isolate the synapse and boost local processing (e.g. *Miller et al. 1985; Spruston 2008*). Indeed, we have gathered evidence that

48 unitary postsynaptic potentials in GC spines are electrically compartmentalized and thus can
49 locally activate voltage-gated Na^+-channels (Na_vs) which in turn activate classic presynaptic
50 high-voltage activated Ca^{2+}-channels (HVACCs) within the spine ('spine spike', *Bywalez et*
51 *al. 2015*). Thus, the reciprocal spine might operate as a mini-neuron that can generate
52 synaptic output upon local activation (*Egger & Urban 2006*).
53 While there have been many earlier studies of recurrent dendrodendritic inhibition at the
54 MTC-GC synapse, it is so far unknown whether a unitary, purely local activation of the
55 spine's microcircuit can indeed trigger release of GABA back onto the exciting MTC. The
56 issue is still unresolved for two reasons:
57 (1) most earlier studies used a strong stimulation of voltage-clamped MCs, namely a
58 depolarization to 0 mV for 20-50 ms *(Isaacson & Strowbridge 1998; Halabisky et al. 2000;*
59 *Isaacson 2001; Chen et al. 2000*). This protocol will cause massive release of glutamate from
60 the lateral MC dendrites, invoking glutamate spillover between them (*Isaacson 1999*) and
61 resulting in long-lasting recurrent inhibition of MCs with both synchronous and asynchronous
62 components, the latter with a time constant of ~ 500 ms. Under these circumstances and
63 zero extracellular $[Mg^{2+}]_e$ GC NMDA receptors (NMDAR) were shown to provide postsynaptic
64 Ca^{2+} entry sufficient to trigger release of GABA from the GC spine (also in *Schoppa et al.*
65 *1998*). However, in normal $[Mg^{2+}]_e$ GABA release was mostly abolished by HVACC blockade
66 (*Isaacson 2001*; see Discussion).
67 (2) In spite of these functional demonstrations of recurrent inhibition and of substantial
68 ultrastructural evidence that GC spines onto MCs are usually reciprocal (e.g. *Price & Powell*
69 *1970, Jackowski et al. 1978, Woolf et al. 1991*), functional connectivity between individual
70 GCs and MCs has remained elusive: no reciprocal connectivity was reported from paired
71 recordings of MCs coupled to GCs so far (*Isaacson 2001, Kato et al 2013, Pressler &*
72 *Strowbridge 2017*) and others including our group have been unable to find connected GC →
73 MC pairs in the first place (see *Egger et al. 2003, Schoppa 2006*). This puzzling observation
74 indicates that paired recordings are not a suitable tool to investigate reciprocal release of
75 GABA.
76 Here we aim to determine whether – and possibly how - single inputs from MC lateral
77 dendrites to single GC spines can also trigger recurrent release of GABA from the reciprocal

78 synapse, using recordings from fluorescently labeled MCs and two-photon uncaging (TPU) of
79 glutamate along their lateral dendrite near Venus-tagged GC spines. TPU of glutamate
80 allows to study the operational mechanisms of the reciprocal microcircuit in single GC spines
81 without causing broader GC activation (*Bywalez et al. 2015*, see also Fig. S1). In this study
82 we use TPU at GC spines to investigate the reciprocal output by the GABAergic release
83 machinery via recording of IPSCs in mitral cells. Thus, processing within a single spine can
84 be disentangled in space and time from extended activation, in order to test the main
85 predictions from our previous study: The mini-neuron hypothesis along with the GC spine
86 spike phenomenon suggest that, just like in conventional axons, Na_v and ensuing HVACC
87 activation are required to cause release, and that unitary activation of the spine is sufficient
88 for triggering release.
89 While this concept is validated here, our study also reveals that presynaptic NMDARs gate
90 reciprocal output at the single-spine level. What is the advantage of such an arrangement
91 compared to classical neuronal processing? In olfactory coding, a large number of input
92 channels needs to be combined to synthesize an olfactory percept (e.g. *Mori et al. 1999,*
93 *Murthy 2011*). We propose that the mechanisms revealed here can explain the conspicuous
94 apparent lack of functional reciprocal connectivity mentioned above and, more importantly,
95 might allow reciprocal GC spines to play a central role in the efficient binding of changing
96 sets of activated input channels and their glomerular columns.
97
98 ***Results***
99 *Experimental configuration*
100 To enable pharmacological interference with components of the reciprocal microcircuit such
101 as Na_vs and HVACCs, we bypassed release from the MC presynapse via TPU of DNI-caged
102 glutamate (DNI, see Methods; *Chiovini et al. 2014; Bywalez et al. 2015; Palfi et al. 2018*) in
103 acute juvenile rat olfactory bulb slices, while recording from MCs in somatic whole-cell
104 voltage-clamp. To visualize the lateral dendrites, MCs were filled with the dye Alexa594 (50
105 μM). Fig. 1A shows the recording configuration.
106 In all MC recordings we observed a high basal frequency of spontaneous events which is a
107 general hallmark of the olfactory bulb network *(Egger & Urban 2006*). Wash-in of 1 mM DNI

108 further increased the basal frequency by on average 1.9 ± 1.2 times (mean value before DNI:
109 4.5 ± 2.1 Hz, n = 14 MCs, P < 0.01), due to the disinhibition resulting from a partial blockade
110 of $GABA_A$Rs by DNI, which also reduced the mean spontaneous IPSC amplitude to a fraction
111 of 0.47 ± 0.16 of control (n = 14 MCs, P < 0.001, Fig. S1 A,B,C). In the presence of DNI, the
112 $GABA_A$R antagonist bicuculline (BCC, 50 μM) blocked spontaneous activity almost
113 completely (frequency: 0.13 ± 0.10 of control, n = 6 MCs, P < 0.01, Fig. 1C, Fig. S1A).

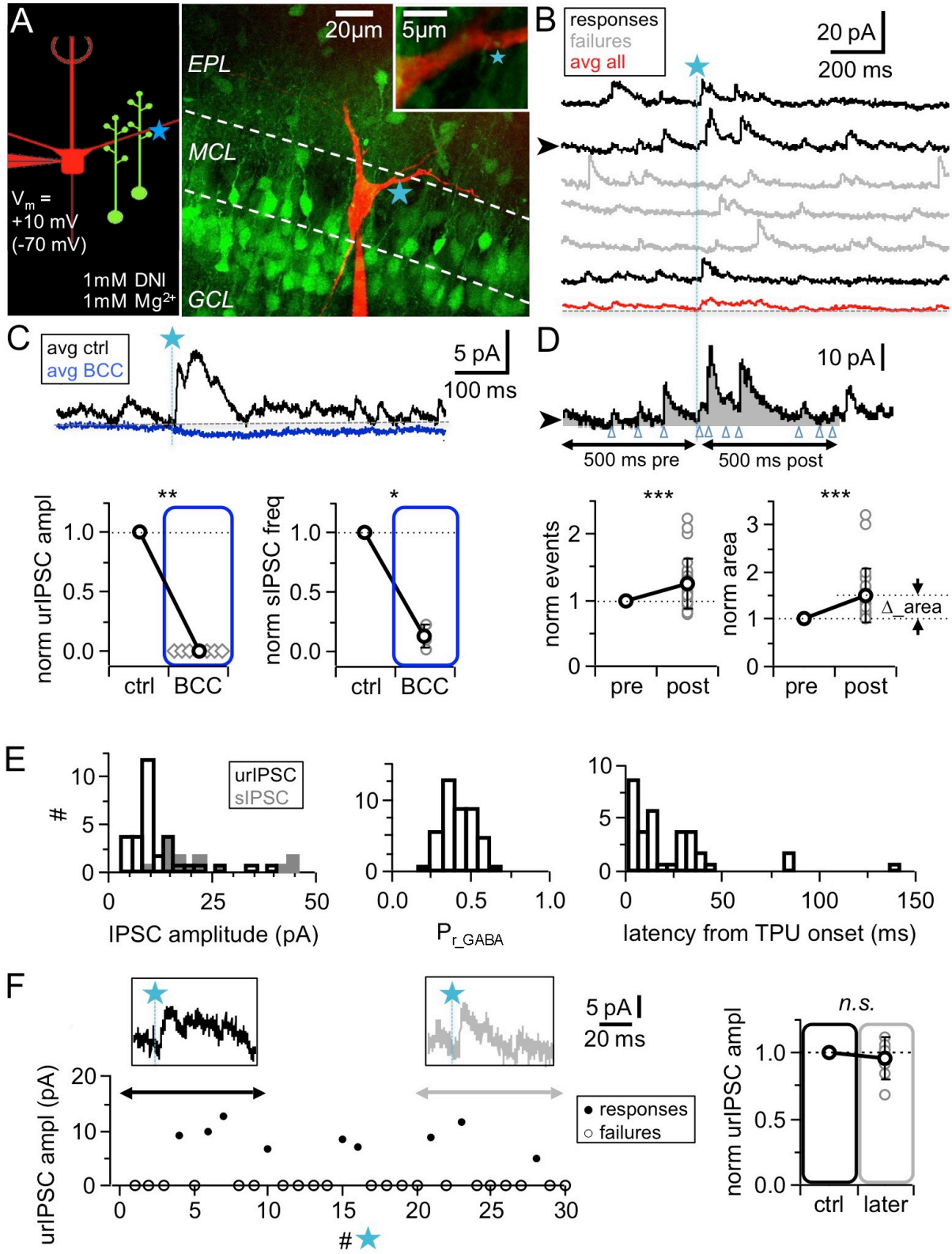

Figure 1. **TPU-induced glutamatergic activation of GC spines triggers GABA release detected as uncaging-evoked reciprocal IPSCs (urIPSCs) in MCs.**

(**A**) Experimental setting (scheme and image): Somatic whole cell voltage clamp recording from MC filled with Alexa 594 (red, 50 µM) and TPU of DNI-caged glutamate (DNI; blue star) at GC spines in VGAT-Venus rats (GCs green).

(**B**) Example of consecutive uncaging traces showing urIPSC responses (black) and failures (grey); average of all recordings shown below (red).

(**C**) Effect of $GABA_AR$ blockade (bicuculline, BCC, 50 µM, blue) on urIPSCs and spontaneous activity. Top: Example experiment, showing averaged traces. Bottom: Cumulative data on urIPSC amplitude (left panel, n =7 MCs) and on frequency of spontaneous IPSCs (right panel, n = 6 MCs).

(D) Analysis of asynchronous events. Top: Example trace from (B) with analysis intervals pre- and

post-uncaging (grey areas, black arrows). Counted events marked by blue arrowheads. Bottom: Normalized IPSC event number and area (integrated activity, relative increase vs control Δ) in pre- versus post-uncaging intervals (n = 27 MCs, see Methods).
(**E**) Properties of first detected triggered urIPSCs (see Methods). Left: Amplitudes (n = 32 MCs, V_m = +10 mV). Dark grey: Amplitude distribution of spontaneous IPSCs for comparison (n = 14 MCs, mean amplitudes). Middle: Release probabilities P_{r_GABA} (n = 44 MCs). Right: Latencies from TPU onset (n = 36 MCs).
(**F**) Stability of urIPSC recordings. Left: Representative experiment showing individual urIPSC amplitude values over consecutive stimulations (1 TPU per min). Insets: Averaged urIPSC responses in the first (black, n = 3 responses) and last ten minutes (grey, n = 3 responses). Right: Comparison of averaged normalized urIPSC amplitudes separated by 10 min interval (n = 7 MCs).
All Figures: Significance (non-parametric tests): n.s. not significant, * $P < 0.05$, ** $P < 0.01$, *** $P < 0.001$; mean data ± S.D.

Since in initial experiments we occasionally observed activation of both NMDA and AMPA autoreceptors on MC dendrites at a holding potential of -70 mV, MCs were clamped to +10 mV in the main body of experiments, near the reversal potential of ionotropic glutamate receptors (*Isaacson 1999; Friedman & Strowbridge 2000*). All experiments were performed at physiological levels of $[Mg^{2+}]_e$ (1 mM).

Triggering of reciprocal IPSCs via TPU

To prevent overstimulation with glutamate, we uncaged with similar laser parameter settings (see Methods) as in the previous study , in which TPU-evoked GC Ca^{2+} signals were indistinguishable from those of unitary spontaneous or triggered synaptic inputs, including their strict localization to the spine head (*Bywalez et al. 2015*), and routinely tested these settings; to ensure similar laser power across experiments, uncaging sites were located at a shallow depth no more than 20 – 30 µm below the surface of the tissue (see Methods). In most experiments, uncaging was performed at one spot in the immediate vicinity of GC spines that were visible in VGAT-Venus rats and in close proximity (0.2 – 0.5 µm) to the MC lateral dendrite (e.g. Fig. 1A, 2A); in a few initial experiments in WT rats uncaging was performed 'blindly' at up to four spots along the dendrite to increase the likelihood for triggering a unitary response (e.g. Fig. 2B; 18% of experiments, see Methods). Responses were detectable in ~ 30% of tested MCs (total n = 166 MCs, see Methods) and in this fraction of MCs would occur only in a small subset of stimulations (see below, Fig. 1F), thus overstimulation of the circuit appears unlikely. In addition, TPU-evoked signals can be expected to be localized to the stimulated GC spine: there is no Ca^{2+} influx into the adjacent dendritic shaft upon TPU, as we have shown in GC Ca^{2+} imaging experiments that were

162 performed previously (dye 100 µM OGB-1 ; average amplitudes ratio ΔF/F spine:dendrite
163 46:2 % ΔF/F, *Bywalez et al. 2015*) and also interleaved with the MC recordings in this study,
164 using a low-affinity dye (100 µM OGB-6F, ratio ΔF/F spine:dendrite 24:2, Ona Jodar et al.
165 2020). Finally we also tested via Ca^{2+} imaging, whether neighboring GC spines of the same
166 GC could sense uncaged glutamate (n = 11 spine pairs, average distance between
167 stimulated and non-stimulated spine 4.1 ± 2.2 µm, range 1.5 -6.8 µm, Fig. S1C, D, E). While
168 the mean amplitude $(\Delta F/F)_{TPU}$ in the stimulated spine set $(\Delta F/F)_{TPU}$ = 52 ± 22% was similar to
169 the data set in Bywalez et al. 2015 (P = 0.38, Mann-Whitney test), there were no detectable
170 Ca^{2+} transients in the non-stimulated spines (amplitude 2 ± 2 %, P < 0.002 versus stimulated
171 spine, Fig. S1C, D), and again there was no detectable Ca^{2+} transient in the dendrite in
172 between (mean 1 ± 2 %, Fig. S1C, D). All three compartments (stimulated and non-
173 stimulated spine heads, dendritic shaft) showed similar Ca^{2+} transients in response to
174 somatically evoked action potentials (Fig. S1D). There was no detectable influence of spine
175 head distance on the relative difference in signal size between stimulated and non-stimulated
176 spines (Fig. S1E). Thus in our paradigm TPU can be expected to act in a spine-specific
177 manner.
178 All uncaging spots were located proximally, at distances < 50 µm from the MC soma (Fig
179 S1F). The rationale for this choice was to minimize electrotonic attenuation, since IPSC
180 amplitudes were small (see above). Moreover, proximal stimulation and the use of VGAT-
181 Venus rats should prevent inadvertent stimulation of reciprocal synapses with other
182 interneuron types (see Introduction).
183 TPU of glutamate resulted in consecutive triggered responses and failures in MCs (Fig. 1B).
184 Responses were classified as triggered if they were observed repeatedly within the same
185 time window and showed similar kinetics (see Methods). Next we tested whether these
186 triggered responses were indeed GABAergic by applying the $GABA_AR$ antagonist Bicuculline
187 (BCC, 50 µM), which invariably blocked responses completely (Fig. 1C, n = 7 MCs, P < 0.01,
188 Wilcoxon test). Thus in the following the triggered events are denoted as urIPSCs (**u**ncaging-
189 evoked **r**eciprocal IPSCs).
190 The amplitude of triggered urIPSCs was on average 12 ± 8 pA (in n = 32 MCs clamped to
191 +10 mV, Fig. 1E), which is significantly smaller than the mean amplitudes of spontaneous

192 IPSCs (sIPSCs, n = 14 MCs; 22 ± 12 pA; P < 0.001, Mann-Whitney test, Fig. 1E, S1B). Since
193 sIPSCs are highly likely to mainly originate from the reciprocal MC-GC circuit (see
194 Discussion), this observation further argues against overstimulation with glutamate in our
195 experiment.
196 The average release probability from the reciprocal spine was estimated as P_{r_GABA} = 0.34 ±
197 0.11 (Fig. 1E, range 0.13 - 0.60, based on n = 44 MCs, see Methods and Discussion). The
198 latencies of urIPSPCs were not normally distributed (Fig. 1E), with a first peak within the first
199 10 ms post TPU onset (n = 13 MCs), a second peak around 30 ms (n = 19 MCs within the
200 range 10-50 ms) and a yet more delayed tail (n = 3 MCs, see Fig. S1H and Discussion).
201 In most experiments we detected putative asynchronous urIPSCs following the first triggered
202 event which were quantified via integral analysis and counting of events (Fig. 1D, see
203 Methods and Discussion). Both area and number of events increased highly significantly in
204 the 500 ms interval following TPU ('post') compared to the same interval right before ('pre';
205 mean increase of integrated activity Δ_area + 0.50 ± 0.55 relative to 'pre' value; mean
206 increase in event number + 0.25 ± 0.37 relative to 'pre' value; n = 27 MCs, P < 0.001 for
207 both; absolute values in 'pre' area 2.40 ± 1.83 pAs, event numbers 26.1 ± 14.9). Δ_area was
208 also significantly increased if the extra area of the synchronous urIPSC was subtracted (P <
209 0.005). The total duration of recurrent inhibition was on average 179 ± 137 ms (range 32 –
210 533 ms, n = 26 MCs, Fig. S1G). Thus, asynchronous recurrent inhibition can be already
211 triggered by single glutamatergic inputs.
212 Sufficient stability of urIPSC responses was established via long-term recordings (see
213 Methods). The amplitudes of averaged responses during the first and last 5 - 10
214 photostimulations (with at least 10 min in between to mimic the time course of
215 pharmacological manipulations, mean number of responses per averaged urISPC 2.8 ± 1.1)
216 were not significantly different (Fig. 1F, n = 7 MCs, ratio last to first 0.95 ± 0.15,P = 0.74).
217
218 From all these experiments we conclude that local, unitary-like TPU of glutamate can stably
219 trigger both fast and slow reciprocal release of GABA, providing proof that the reciprocal
220 microcircuit can be activated by single synaptic inputs at physiological levels of Mg^{2+}.

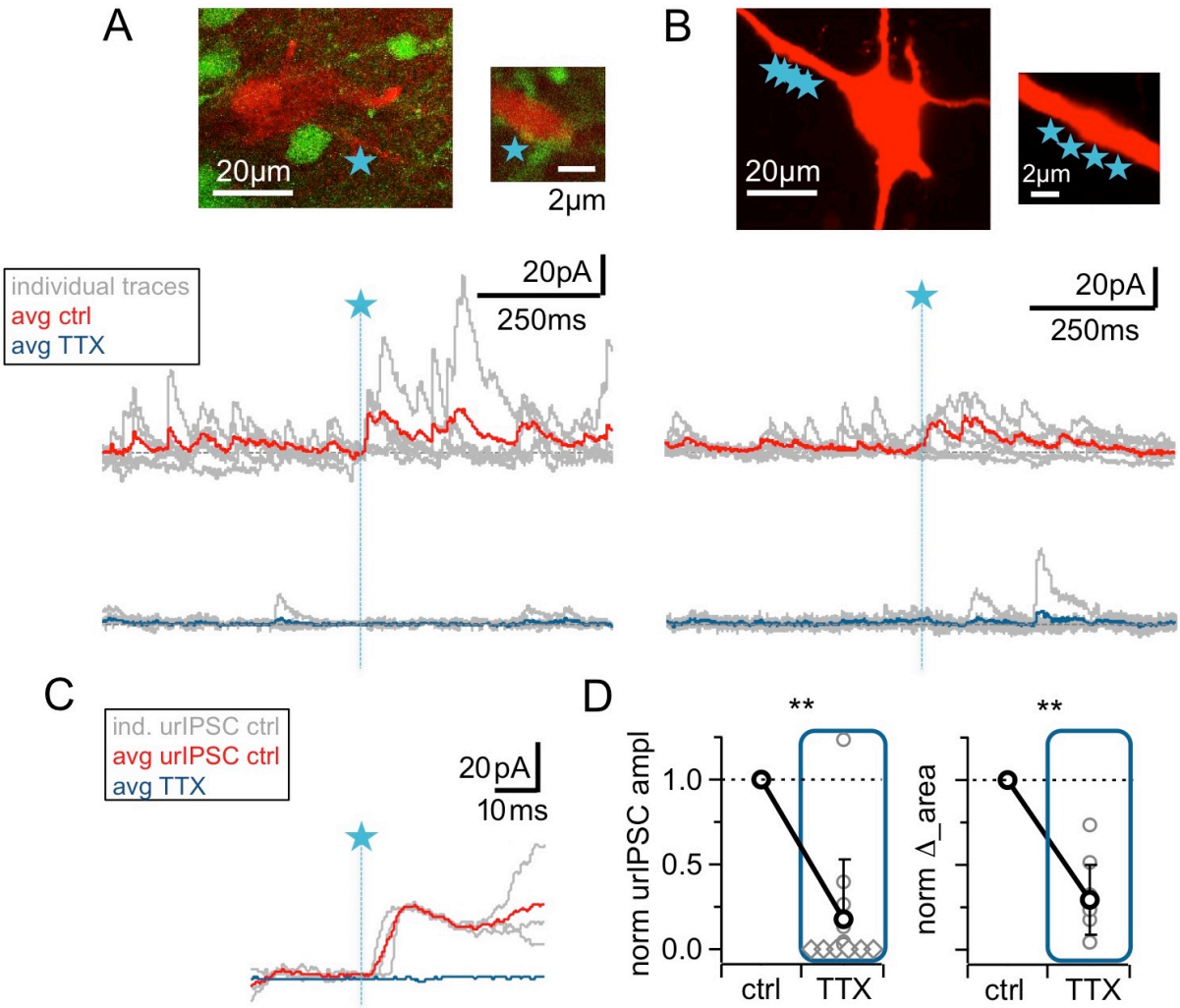

Figure 2. The urIPSC is reduced by Na_v blockade (TTX, 500 nM).
(**A, B**) Representative experiments showing a patch-clamped mitral cell (Alexa594 50 µM, red), the uncaging site(s) along a lateral dendrite (blue star) and below the corresponding uncaging traces with individual traces shown in grey, average control traces in red and average TTX traces indicated in blue (A: VGAT-Venus rat, single-site TPU, B: Wistar rat, multi-site TPU). The average traces contain all recordings, both with and without detected responses.
(**C**) Magnified illustration of traces in (A) (for control individual traces with urIPSC responses and their average, for TTX only average, color coding as above).
(**D**) Left: Cumulative normalized data showing the strong reduction of urIPSC amplitude during Na_v blockade with TTX (n = 12 MCs). Diamonds indicate the experiments with no detectable response in the presence of the drug. Right: Comparison of normalized IPSC Δ_area between control and in the presence of TTX (see Methods, n = 10 MCs).

Sodium channel activation is required for most urIPSCs

Next, we investigated a possible contribution of the GC spine spike and thus Na_v activation to urIPSC generation. Fig. 2 illustrates that wash-in of TTX (500 nM) substantially reduced both triggered and spontaneous events. On average, urIPSC amplitudes were reduced to a fraction of 0.17 ± 0.34 of control (Fig. 2D, n = 12 MCs, $P < 0.005$, Cohen's d = 2.54; absolute control amplitudes for -70 mV: -7.8 ± 3.6 pA, n = 5 MCs; for +10 mV: 15.4 ± 12.4 pA, n = 7 MCs), and the increase in integrated activity Δ_area was decreased to 0.28 ± 0.21 of its

242 control value (see Methods; Fig. 2D, n = 10 MCs, P < 0.005). While the frequency of
243 spontaneous activity was also strongly decreased in TTX, to a fraction of 0.24 ± 0.17 of
244 control (Fig. S2B, n = 10 MCs, P < 0.005), the mean sIPSC amplitude was unchanged by
245 TTX (1.36 ± 0.68 of control, n.s., n = 10 MCs, Fig. 2A,B, Fig. S2A, B). There was no
246 significant correlation between the TTX-induced reductions in sIPSC frequency and in
247 urIPSC amplitude (Fig. S2C, n = 10, r = 0.23, P = 0.26). Thus the reduction in urIPSC
248 amplitude is unlikely to be directly related to network effects of TTX.
249
250 Thus Na_vs are essential to trigger GABA release from the reciprocal spines.

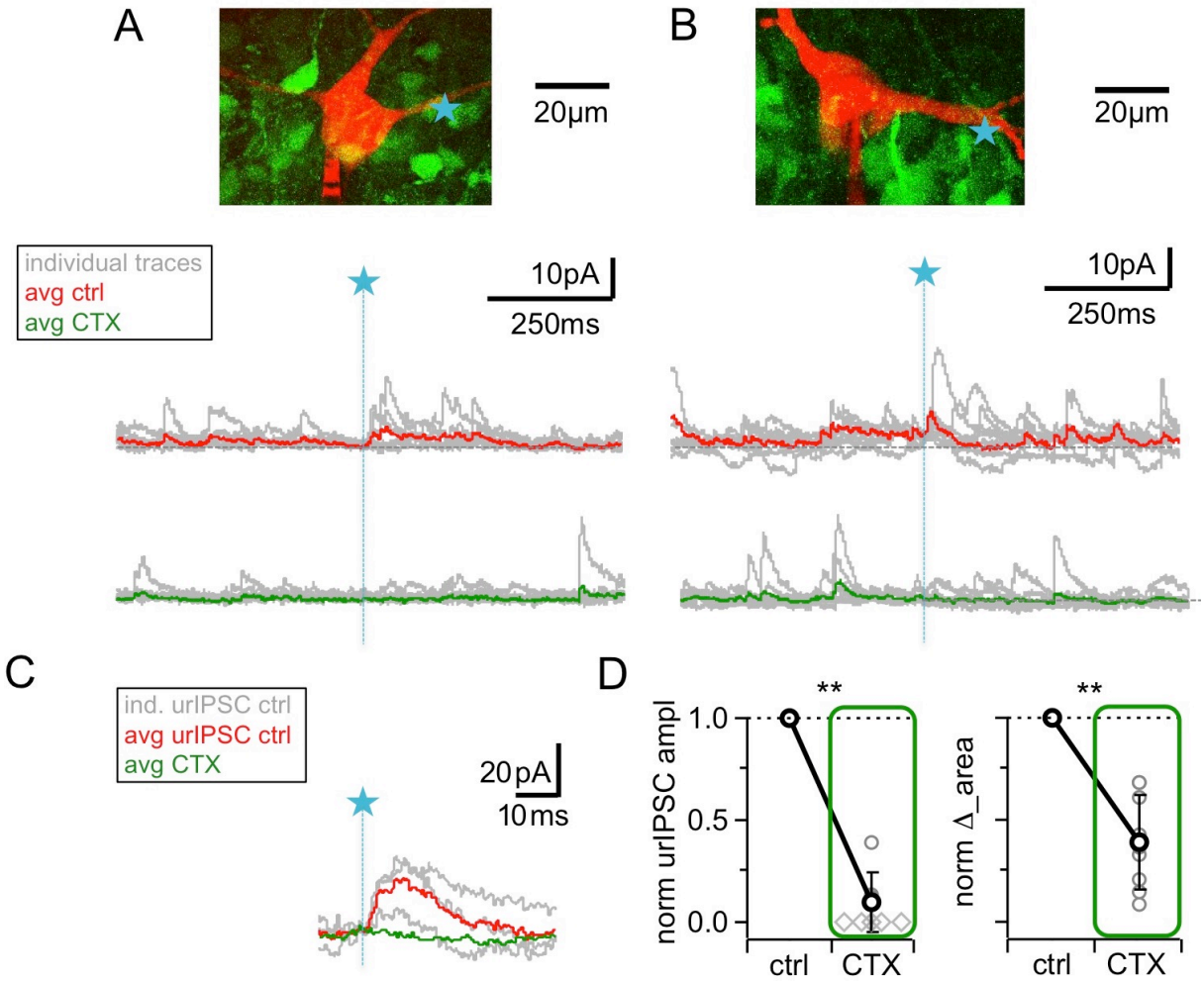

251
252 **Figure 3. Blockade of high voltage activated Ca^{2+}-channels by ω-conotoxin MVIIC (CTX, 1**
253 **µM) causes a prominent reduction of urIPSC amplitudes.**
254 (**A, B**) Two representative experiments in brain slices from VGAT-Venus rat with the corresponding
255 MC (red), the site of TPU (blue star) and the uncaging traces according to the condition (individual
256 traces : grey, average control: red, average CTX: green). The average traces contain all recordings,
257 both with and without detected responses. Left: same cell as in Fig. 1B.
258 (**C**) Magnified illustration of traces in B (for control individual traces with urIPSC responses and their
259 average, for CTX only average, color coding as above).
260 (**D**) Left: Summary of effects of CTX on average normalized urIPSC amplitude (n = 8 MCs).
261 Diamonds indicate the experiments with no detectable response in the presence of the drug. Right:

262 Comparison of delta urIPSC areas normalized to control versus in the presence of CTX (n = 9 MCs).

263 *High-voltage activated Ca^{2+} channels in the spine trigger GABA release*

264 HVACCs have been implied to mediate recurrent release from reciprocal spines (*Isaacson*
265 *2001*) and are activated by Na_vs, contributing a substantial fraction to the total postsynaptic
266 Ca^{2+} signal in the GC spine (*Bywalez et al. 2015*). To directly test whether HVACC activation
267 is required for release of GABA, we blocked NPQ-type Ca^{2+} channels with 1 μM ω-conotoxin
268 MVIIC (CTX; *Bloodgood & Sabatini 2007; Bywalez et al. 2015*).

269 Fig. 3 shows the resulting substantial decrease of urIPSCs, to a fraction of 0.08 ± 0.14 of
270 control (from a mean amplitude of 11.3 ± 5.7 pA; n = 8 MCs, P < 0.005, Cohen's d = 6.6, Fig.
271 3D). This decrease was not different from the effect of TTX on urIPSC amplitude described
272 above (P = 0.35, ratios in CTX vs TTX). Δ_area decreased to 0.39 ± 0.23 of control (n = 9
273 MCs, P < 0.005, Fig. 3D), again statistically not different from the effect of TTX on Δ_area
274 described above (P = 0.15 vs TTX).

275 CTX decreased sIPSC frequency to a fraction of 0.53 ± 0.15 of control, less markedly than
276 TTX (Fig. 3E, n = 7 MCs, control vs CTX: P < 0.01; CTX vs TTX: P < 0.005), and had no
277 effect on the mean sIPSC amplitude (Fig. 3A,B; Fig. S3A, B; 1.00 ± 0.12 of control, n = 7
278 MCs, n.s.). There was no significant correlation between the CTX-induced reductions in
279 sIPSC frequency and in urIPSC amplitude (Fig. S3C, n = 7, r = -0.38, P = 0.19).

280 We conclude that HVACC activation is required for release of GABA from the reciprocal
281 spine following local input.

282 *NMDA receptors are also relevant for recurrent release*

283 NMDARs are known to substantially contribute to unitary synaptic transmission and to
284 postsynaptic Ca^{2+} entry at the MC to GC synapse (*Isaacson & Strowbridge 1998; Schoppa et*
285 *al. 1998; Isaacson 2001; Egger et al. 2005*). However, because of our previous observation
286 that NMDAR-mediated Ca^{2+} entry into GC spines did not depend on Na_v activation (in
287 contrast to HVACC-mediated Ca^{2+} entry, *Bywalez et al. 2015*), and because of the strong
288 blocking effects of TTX or CTX on urIPSCs reported above, we expected that NMDAR
289 blockade would have only mild effects on fast recurrent release upon single inputs.
290 Intriguingly however, Fig. 4A-D shows that the application of 25 μM D-APV resulted in a
291 substantial decrease of urIPSC amplitudes, to on average 0.22 ± 0.21 of control (from a

292 mean amplitude of 13.8 ± 8.6 pA, n = 10 MCs, P < 0.002, Cohen's d = 3.7, Fig. 4D). All
293 individual experiments showed the amplitude decrease, albeit to a variable degree (range
294 0.00 - 0.68 of control). Δ_area following TPU decreased to 0.40 ± 0.28 of control (n = 10
295 MCs, P < 0.003, Fig. 4D). Both effects were statistically not different from the effects of either
296 TTX or CTX (amplitude: P = 0.12 and P = 0.08; Δ_area: P = 0.19 and P = 0.47).
297

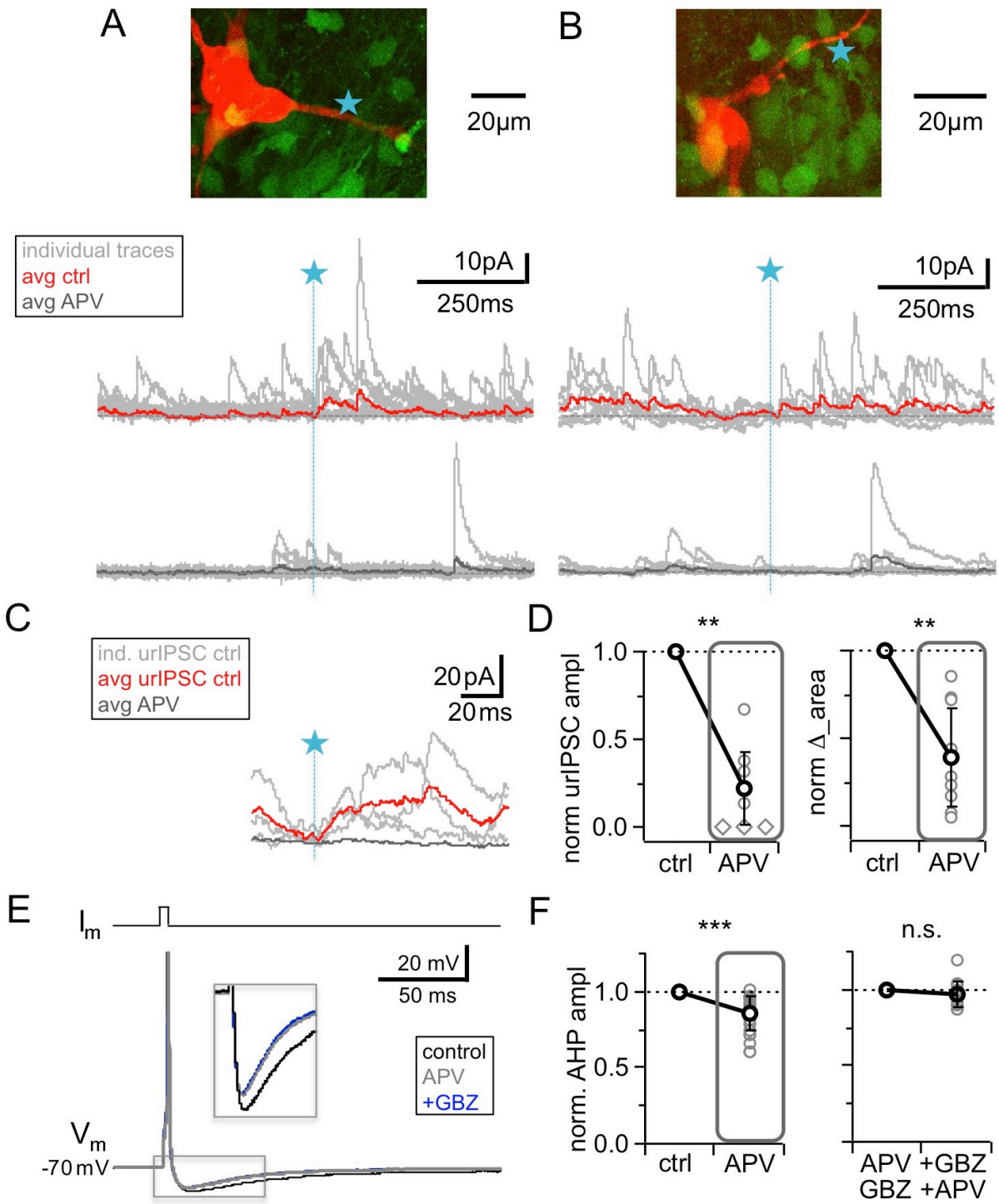

Figure 4. NMDAR blockade with D-APV (25 µM) results in a strong reduction of urIPSC amplitudes and also reduces AHPs following mitral cell APs

(**A, B**) Two representative uncaging experiments with the corresponding MC (red), the site of TPU (blue star) and the uncaging traces according to the condition (individual traces: grey, average control: red, average APV: dark grey); both VGAT-Venus. The average traces contain all recordings, both with and without detected responses.

(**C**) Magnified illustration of traces in A (for control individual traces with urIPSC responses (grey) and their average (red), for APV only average (dark grey)).

(**D**) Left: Summary of effects of APV on average normalized urIPSC amplitude (n = 10 MCs). Diamonds indicate the experiments with no detectable response in the presence of the drug. Right: Comparison of delta urIPSC integrals between control versus in the presence of APV (n = 10 MCs).

(**E**) Representative example of MC AP evoked by somatic current injection in control conditions (black trace) and in the presence of APV (grey trace) and added GBZ (20 µM; blue trace). Inset: Magnified afterhyperpolarizations (AHPs)s.

(**F**) Left: Cumulative effects of APV on average normalized AHP amplitude (n = 18 MCs). Right:

Effect of occlusion experiments on AHP amplitude (APV before GBZ or GBZ before APV, n = 12 MCs).

While APV also substantially reduced sIPSC frequency, to 0.27 ± 0.23 of control (n = 10 MCs, P < 0.005, Fig. 4A, B; Fig. S4A, B), similar to TTX (P = 0.79) and significantly more pronounced than CTX (P < 0.01), the mean sIPSC amplitude was unchanged (Fig. 4A, B; Fig. S4A, B; 0.93 ± 0.29 of control, n = 10 MCs, P = 0.19). There was no positive correlation between the APV-induced reductions in sIPSC frequency and urIPSC amplitude (Fig. S4C, n = 10, r = -0.23, P = 0.26). Therefore network effects of APV are unlikely to explain the strong reduction of urIPSC amplitude.

Since the strength of the effect of NMDAR blockade on urIPSCs was surprising to us, we sought to provide another line of evidence for these findings in an experimental setting that does not involve uncaging of glutamate (which might preferentially activate NMDARs, see Discussion). The afterhyperpolarization (AHP) following single MC APs elicited by somatic current injection was found to mainly reflect recurrent inhibition in brain slices from adult mouse (*Nunes & Kuner 2018*), while in juvenile rat inhibitory synaptic contributions to the AHP were observed to be less substantial but still detectable (on the order of 20-30% relative to the K^+ channel-mediated component, *Dumenieu et al. 2015*). We used this paradigm to test whether NMDAR blockade alone could interfere with recurrent inhibition (Fig. 4E, F). Single MC AP AHPs (V_{hold} = -70 mV) had a mean amplitude ΔV_m = – 9.2 ± 2.2 mV (n = 18) and a mean half duration $t_{1/2}$ = 43 ± 25 ms (n = 13). Fig. 4F shows that APV application significantly reduced the mean AHP amplitude to a fraction of 0.86 ± 0.11 of control (P < 0.0001, Wilcoxon test, Cohen's d = 0.86; reduction in 17 of 18 MCs), while the half duration was not changed (fraction of control 1.02 ± 0.42, P = 0.65, not shown). Next, to block $GABA_A$Rs we turned to gabazine (GBZ, 20 µM), since Bicuculline might affect the K^+ channels that contribute to slow AHPs (*Khawaled et al. 1999, Dumenieu et al. 2015*). GBZ alone caused a slightly stronger reduction than APV, which was not significantly different (to 0.71 ± 0.10 of control, n = 7 MCs, P = 0.08 vs APV, not shown). Occlusion experiments using APV before GBZ or GBZ before APV did not result in any further reduction (0.97 ± 0.09 of

344 amplitude in presence of first drug, n = 12 MCs, P = 0.16, Fig. 4E, F). Thus these
345 experiments also support a substantial role of GC NMDARs for GABA release.
346 From these and the uncaging experiments we conclude that NMDARs located on GCs are
347 strongly involved in reciprocal release, even though prevention of HVACC activation (via Na_v
348 block or pharmacology) also blocks reciprocal release. What is the underlying mechanism?
349 The simplest explanation for a cooperation would be a summation of NMDAR- and HVACC-
350 mediated Ca^{2+} currents at the presynaptic Ca^{2+} sensor. For this scenario two requirements
351 need to be satisfied: (1) temporal overlap of Ca^{2+} currents and (2) spatial proximity of
352 NMDARs and HVACCs within the same microdomain.
353 *Temporal overlap: Simulations of GC spine Ca^{2+} currents via HVACCs and NMDARs*
354 In conventional glutamatergic synapses the NMDAR-mediated postsynaptic current is rising
355 rather slowly compared to the AMPAR-mediated component (rise time ~ 10 ms, *Lester et al.*
356 *1990*) and therefore the fractional NMDAR Ca^{2+} current seems at first an unlikely candidate
357 to make direct contributions to fast release. In the reciprocal GC spines however, Na_v
358 channels are locally activated, which enables fast and substantial NMDAR activation. Fig. 5A
359 shows a simulation of the postsynaptic NMDAR- and HVACC-mediated Ca^{2+} currents (based
360 on the detailed NEURON model described in *Aghvami et al. 2019*, see Methods) which
361 illustrates that the local AP causes a transient boosting of the NMDAR Ca^{2+} current because
362 of further relief of the Mg^{2+} block during the upstroke and overshoot of the spine spike.
363 According to the simulation this fast NMDAR-mediated Ca^{2+} spikelet begins even before the
364 HVACC-mediated current and tightly overlaps with it within > 1 ms. Thus HVACC- and
365 NMDAR-mediated Ca^{2+} currents could act in a cooperative manner at the Ca^{2+} sensor(s) that
366 mediate fast release of GABA, especially so, if the release probability was proportional to the
367 fourth power of local $\Delta[Ca^{2+}]$ or more as at other central synapses, and if the channels were
368 close enough to form a microdomain, allowing for an 'overlap bonus' (*Stanley 2016*; Fig. 5B).
369 In the temporal domain, this overlap was found to be highly robust against the variation of the
370 combined Na_v/K_v conductance, and increases in either AMPAR conductance g_{AMPA} or neck
371 resistance R_{neck} resulted in an earlier activation of both HVACC and NMDAR-mediated Ca^{2+}
372 currents and even stronger overlap (Fig. 5C, see Methods). Decreases resulted at first in
373 little change and then a loss of the spine spike whereupon there is no more HVACC

activation. To illustrate specifically the contribution of the Na_v-mediated boosting of the NMDAR-mediated Ca^{2+} current, we also calculated the overlap bonus for the HVACC-mediated current as above and the NMDAR current in absence of the spine spike, which indeed renders the cooperative effect negligible (Fig. 5B).

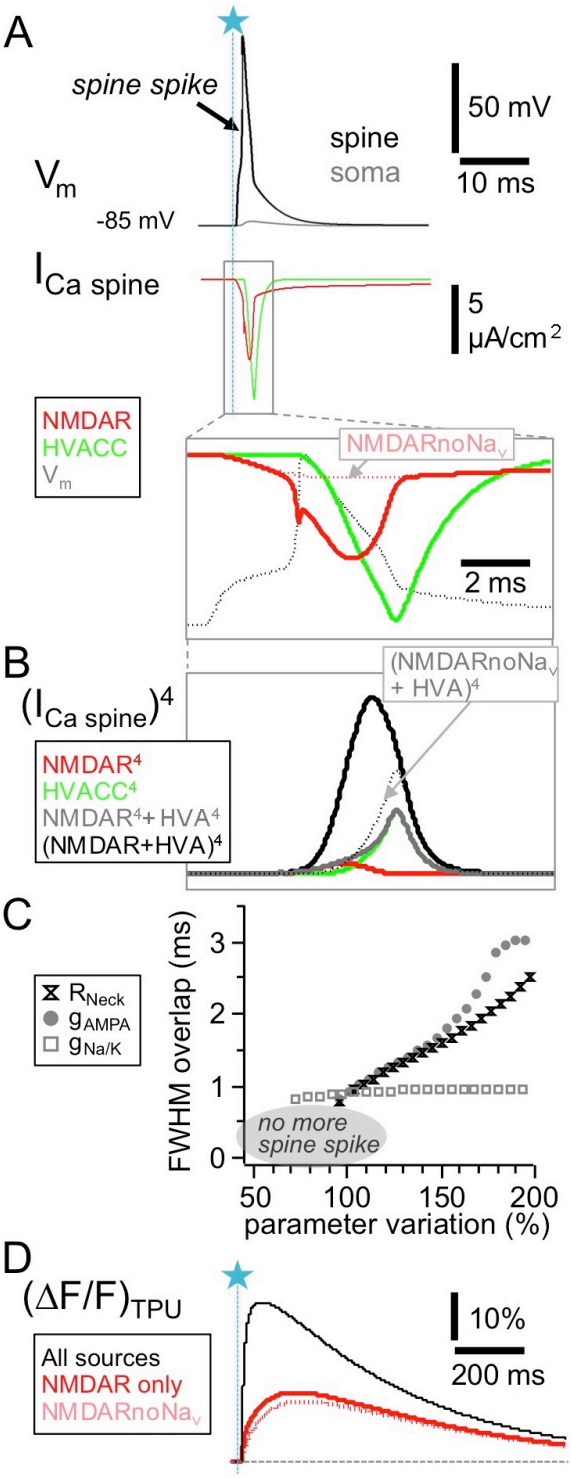

Figure 5. HVACC- and NMDAR-mediated Ca^{2+}-currents overlap temporally in the wake of the spine spike. Simulated spine Ca^{2+}-currents and $(\Delta F/F)_{TPU}$

(**A**) Top panels: spine membrane potential V_m and Ca^{2+}-currents (parameters exactly as in *Aghvami et al. 2019*, their Fig. 2B, except for removed exogenous Ca^{2+} buffer). Bottom: Blow-up of NMDAR- and HVACC-mediated Ca^{2+}-currents, overlaid with the membrane potential V_m. Note the early onset of the NMDAR Ca^{2+}-current and its increase during the underlying local action potential. Red dotted line: NMDAR Ca^{2+}-current in the absence of Na_vs.

(**B**) The temporal coincidence creates an ‚overlap bonus' with respect to local Ca^{2+} concentration and triggering of release: Fourth power of single and added Ca^{2+}-currents. Black dotted line: Addition of HVACC with NMDAR Ca^{2+}-current in the absence of Na_vs (purely hypothetical: pretending that HVACC was not affected, only the NMDAR Ca^{2+}-current).

(**C**) Robustness test for extent of overlap between NMDAR- and HVACC-mediated Ca^{2+}-current. Overlap is measured as the stretch of overlapping FWHMs of the current transients (Full Width Half Maxima, see Methods). Parameter variation within 50 - 200% of the nominal value of the neck resistance R_{neck}, the AMPAR conductance gAMPA and the coupled Na_v/K_v conductance $g_{Na/K}$. Results are shown only for parameter runs with spine spike.

(**D**) Simulated fluorescence transients ΔF/F (in the presence of 100 µM OGB-1) show that the contribution of the Na_v-mediated boost of NMDAR Ca^{2+}-currents to the total NMDAR-mediated Ca^{2+} signal is almost negligible (see Discussion).

Spatial proximity: Ultrastructural evidence for presynaptic localization of NMDARs

For fast neurotransmitter release to occur, the current view is that Ca^{2+} entry needs to happen in a proximity of 100 nm or less from the Ca^{2+} sensing part of the SNARE machinery

382 (reviewed in *Kaeser & Regehr 2014; Stanley 2016*). Therefore, to permit cooperation of Ca^{2+}
383 influxes, NMDARs should be localized very close to or within the GABAergic presynapse.
384 Earlier electron microscopic (EM) studies had reported the presence of postsynaptic
385 NMDARs in GC spines and also instances of extrasynaptic labeling (*Sassoè-Pognetto &*
386 *Ottersen 2000, Sassoè et al. 2003*). To test for the presence of NMDARs near or within
387 GABAergic active zones, we analysed GC spine heads in ultrathin sections that were
388 immunogold-labeled with either GluN1 or GluN2A/B antibodies (Fig. 6A; see Methods); the
389 sections were selected for the presence of at least one asymmetric (i.e. glutamatergic)
390 contact and/or one symmetric (i.e. GABAergic) contact.

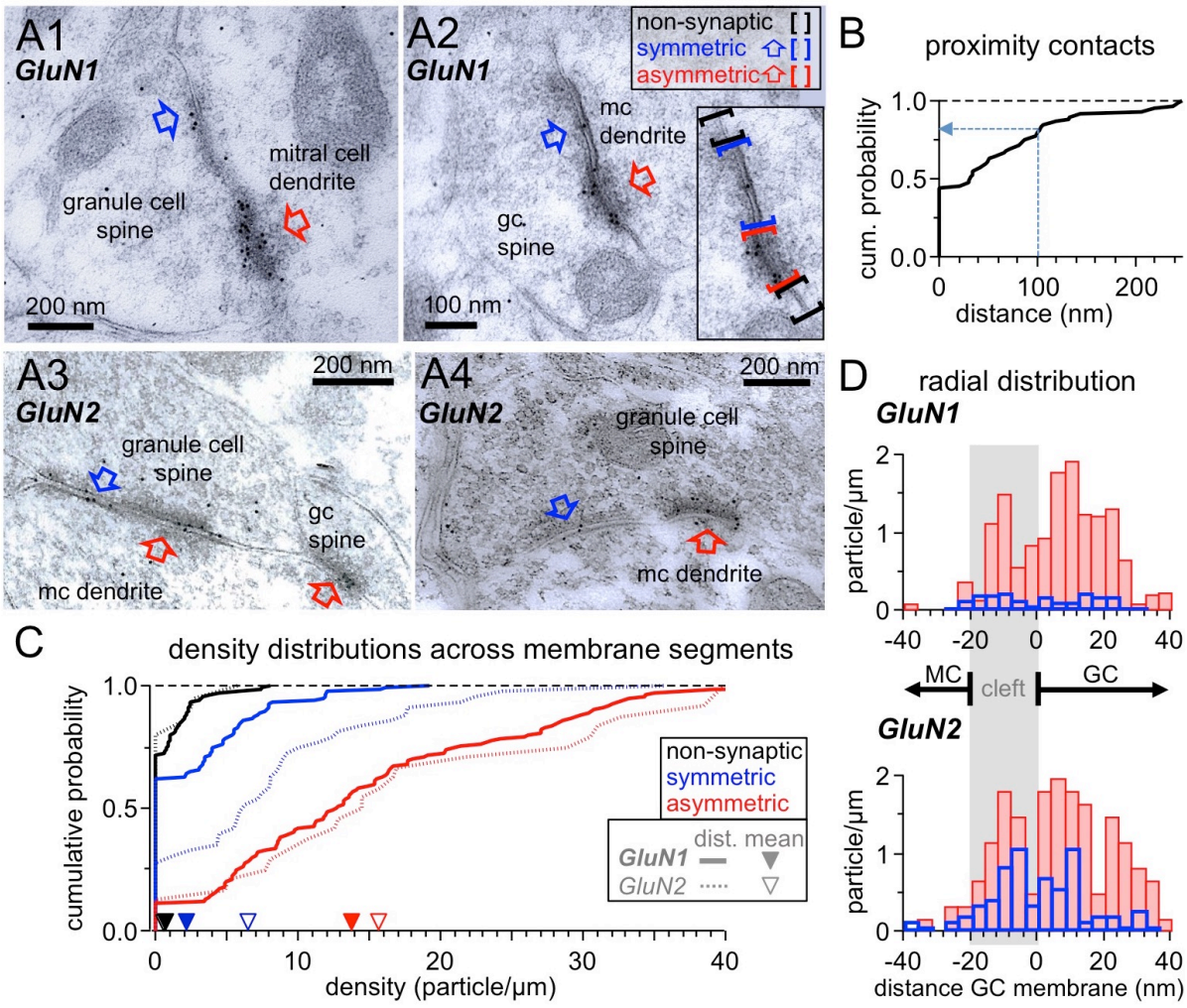

391
392 **Figure 6. Ultrastructural analysis of the distribution of NMDARs shows their presence at both**
393 **post- and presynaptic GC spine membranes in reciprocal dendro-dendritic synapses.**
394 (**A**) Representative micrographs of reciprocal dendrodendritic synapses labeled for GluN1 (A1, A2)
395 and GluN2A/B (A3, A4). Note that asymmetric MC-to-GC synapses (red arrows) are strongly labeled
396 and that symmetric GC-to-MC junctions (blue arrows) are also immunopositive. Gold particles are
397 usually not associated with non-synaptic plasma membrane domains of GC spines. The inset in panel
398 A2 illustrates the selection of non-synaptic membrane segments (black brackets), symmetric synapses
399 (blue) and asymmetric synapses (red).

(**B**) Frequency distribution of distances between symmetric and asymmetric synaptic profiles on the same GC spine membrane (based on n = 60 micrographs with both types of profiles on the same spine).

(**C**) Frequency distributions of labeling densities across synaptic (symmetric and asymmetric) and non-synaptic membrane segments for GluN1 (thick lines, n = 120, 111, 138 segments, respectively) and GluN2A/B (thin dotted lines, n = 46, 25, 24 segments, respectively). The arrows on the x-axis indicate the mean density (GluN1: solid, GluN2A/B: open). Color code as in (A).

(**D**) Radial distribution of gold particles representing GluN1 (top panel) and GluN2A/B (bottom panel) at asymmetric (red) and symmetric (blue) synapses. Particle numbers were normalized to the total length of the respective synaptic segments. Absolute particle numbers see Results.

410 Interestingly, we observed that when both symmetric and asymmetric synaptic profiles were
411 visible in individual GC-MC dendrodendritic pairs, the two synaptic profiles were mostly either
412 contiguous (44% of n = 60 cases, examples Fig. 6A2,A3, cumulative plot Fig. 6B) or closer
413 than 100 nm (36% of cases). This finding implies that on both sides of the dendrodendritic
414 synaptic arrangement the postsynaptic specialization very often merges with presynaptic
415 release sites without interposition of non-synaptic membrane domains, and that therefore on
416 the GC side postsynaptic NMDARs can be located very closely to the GABAergic
417 presynapse.
418 Immunogold labeling for NMDARs was also frequently observed in symmetric contacts, albeit
419 at a lesser density compared to asymmetric contacts (Fig. 6A). To establish whether there is
420 an increased likelihood for the presence of NMDARs at symmetric contacts versus
421 extrasynaptic profiles, we compared the densities of labeling in non-synaptic membrane
422 segments of GC spines with those in symmetric synapses, and as a control in asymmetric
423 synapses. GC spines establishing synapses with MC dendrites were selected as described
424 (see Methods) and all discernible membrane segments within a spine were analysed. For
425 GluN1, there were 50 particles along 84.5 µm of 138 non-synaptic spine membrane
426 segments (mean 0.6 particles/µm), 70 particles along 32.7 µm of 120 symmetric profiles
427 (mean 2.1 particles/µm) and 394 particles along 28.6 µm of 111 asymmetric profiles (mean
428 13.8 particles/µm). Fig. 6C shows the density distributions across the three types of
429 membrane segments. The distribution of the density of gold particles at symmetric synapses
430 was significantly higher than the one in non-synaptic membrane (P = 0.000029, Kolmogorov-
431 Smirnov test). For GluN2A/B, the sample size was smaller, with 5 particles along 10.0 µm of
432 24 non-synaptic spine membrane segments (mean 0.5 particles/µm), 89 particles along 14.0
433 µm of 46 symmetric profiles (mean 6.4 particles/µm) and 96 particles along 6.1 µm of 25
434 asymmetric profiles (mean 15.7 particles/µm). Still, the density distribution at symmetric
435 synapses was significantly higher than the distribution at the non-synaptic membrane (P =
436 0.000048).
437 Interestingly, while the labeling densities for GluN1 and GluN2A/B were similar across non-
438 synaptic membranes and asymmetric synapses each (P = 0.99 and P = 0.81, respectively),
439 labeling of symmetric synapses was considerably stronger for GluN2A/B versus GluN1 (P =

440 0.00042). This difference might be due to a distinct receptor configuration and/or a better
441 accessibility of the GluN2 epitopes in the presynaptic symmetric membrane.
442 Finally, we analysed the radial distribution of particles across synaptic profiles for both
443 antibodies to establish whether labeling was predominantly associated with either the GC or
444 the MC membrane (Fig. 6D; see Methods). The distribution of both GluN1 and GluN2A/B
445 label at asymmetric synapses was similar, with a main peak just inside the postsynaptic GC
446 membrane and another peak within the synaptic cleft. Only a few gold particles were
447 localized beyond 20 nm on the MC side, suggesting that NMDARs are not expressed at
448 significant levels at the glutamate release sites on the MC membrane. Notably, the
449 distribution of gold particles at symmetric synapses mirrored the one at asymmetric
450 synapses, implying that labeling for NMDARs is predominantly associated with both the
451 presynaptic GABAergic and the postsynaptic glutamatergic membrane of GCs.
452 In summary, we conclude from these findings that NMDARs do play a direct presynaptic role
453 for GABA release from the reciprocal spine, albeit in cooperation with HVACCs (Fig.7). A
454 direct consequence of this conclusion is that any inhibitory output from a GC spine will
455 require the presence of glutamate and thus synaptic input to the respective spine (except
456 perhaps for GC action potential bursts), with far-ranging implications for the role of GC-
457 mediated lateral inhibition in early olfactory processing (see Discussion).
458

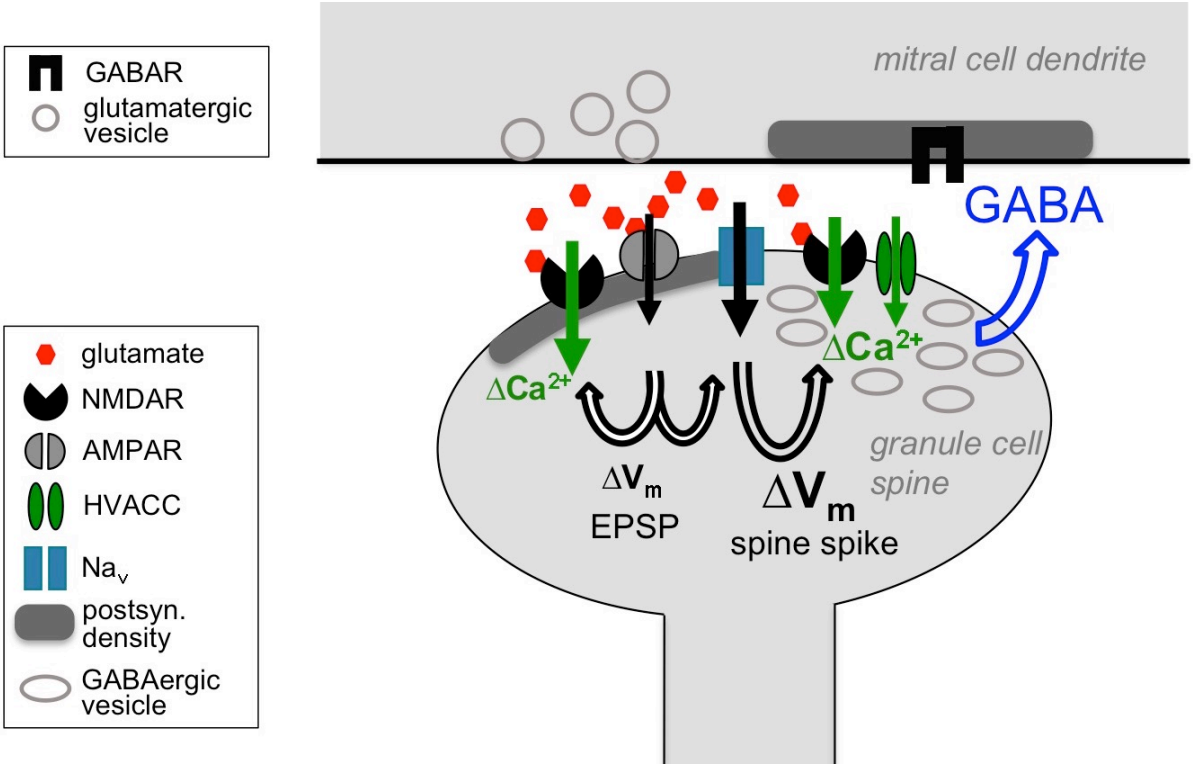

Figure 7 Cooperative release of GABA from the granule cell reciprocal spine
Depolarizing currents are indicated by black solid arrows and Ca^{2+} entry by green solid arrows. Upon release of glutamate from the mitral cell dendrite, AMPARs get activated, leading to depolarization of the spine, then activation of both post- and presynaptic NMDARs and Na_vs. The latter in turn drive further depolarization, i.e. the spine spike, which both activates HVACCs and enhances Ca^{2+} entry via NMDARs by additional relief of their Mg^{2+} block. HVACC- and presynaptic NMDAR-mediated Ca^{2+}-currents cooperate to promote recurrent release of GABA onto the mitral cell dendrite.

469 ***Discussion***

470 Here we have demonstrated that mimicking unitary synaptic inputs via two-photon uncaging
471 of glutamate onto individual olfactory bulb GC spines can activate the entire microcircuit
472 within the spine, from the local spine spike to the release of GABA onto MC lateral dendrites,
473 proving the mini-neuron-like functionality of the reciprocal microcircuit. As in classical axonal
474 release, sequential Na_v channel and HVACC activation triggers output, which occurs on both
475 fast and slow time scales. Strikingly, however, presynaptic NMDA receptors are also found to
476 play a role for GABA release. These findings together with other prior knowledge allow to
477 make an educated guess regarding the specific function of reciprocal spines in bulbar
478 processing (see further below).

479 *Properties of microcircuit operation and implications for coincident local and global activation*

480 For the proximal reciprocal GC inputs investigated here we estimate that under physiological
481 conditions close to the MC resting potential the size of the fast IPSCs is on the order of -5
482 pA, after corrections for the partial $GABA_AR$ block by DNI and the setting of E_{Cl}. Thus,
483 assuming an *in vivo* MC input resistance of 100 MΩ (*Angelo & Margrie 2011*), an inhibitory
484 input from a single GC spine will exert a somatic hyperpolarization of at best 0.5 mV, and
485 therefore even proximal GC inputs will barely influence MC firing (*Fukunaga et al. 2014;*
486 *McIntyre & Cleland 2016*) - unless there is coordinated activity across GC spines connected
487 to the same MC dendrite, for example in the wake of an MC action potential during the
488 recurrent IPSP (see e.g. Fig. 4F) or during gamma oscillations (e.g. *Kay 2003; Lagier et al.*
489 *2004*).

490 Upon local activation we observed a GABA release probability P_{r_GABA} from the GC spine on
491 the order of 0.3. This value might represent an upper limit, because the global reduction of
492 inhibition by DNI could cause a homeostatic upregulation of P_{r_GABA} (e.g. *Rannals & Kapur*
493 *2011*), and the detection of connections is generally biased towards larger P_{r_GABA}. Moreover,
494 it might be developmentally further downregulated, since recurrent inhibition was shown to
495 decrease in older animals (*Dietz et al. 2011; Dumenieu et al. 2015*).

496 With $P_{r_GABA} \approx 0.3$ and the probability for MC glutamate release on the order of $P_{r_Glu} \approx 0.5$ –
497 0.75 (*Egger et al. 2005; Pressler & Strowbridge 2017*) the efficiency of the entire reciprocal
498 microcircuit can be estimated as $P_{reciprocal} = P_{r_Glu} \cdot P_{r_GABA} \approx 0.2$, possibly informing future

499 network models. The rather low P_{r_GABA} observed here also implies that GC spines are likely
500 to release with higher probabilities upon coincident non-local GC signalling (i.e. regional or
501 global Ca^{2+} or Na^{+} spikes), due to substantially increased ΔCa^{2+} in the spine as observed
502 previously (*Egger et al. 2005; Egger 2008; Aghvami et al. 2019; Mueller & Egger 2020)*.
503 Therefore we predict such coincident non-local activity to boost both recurrent and lateral
504 inhibition.
505 As to the minimal latency for recurrent GABA release, the temporal resolution of our
506 experiments is limited by the uncaging laser pulse duration (1 ms) and by the unknown exact
507 time course $V_m(t)_{SPINE}$ of the spine spike. Fig. 1E shows that the fastest urIPSCs were
508 detected within 2 ms from TPU onset, implying that there is a fast mechanism coupling Ca^{2+}
509 entry to release - in line with earlier findings of tight coupling between Ca^{2+} entry and GABA
510 release (using EGTA, *Isaacson, 2001*), and of a crucial role for Na_v channels (*Bywalez et al.*
511 *2015; Nunes & Kuner 2018*) – as also indicated by our simulations (Fig. 5A).
512 While ~ 30% of urIPSCs occurred within 10 ms post TPU onset, there was a substantial
513 fraction with longer latencies in the range of 10 - 30 ms and a few with even larger delays
514 (which might also correspond to false positives of our detection method). Again, since
515 $V_m(t)_{SPINE}$ is unknown, we cannot determine to what extent these urIPSCs were actually
516 asynchronous (if defined as release events that happen later than the fast coupling of HVA
517 presynaptic Ca^{2+} currents to the release machinery, e.g. *Kaeser & Regehr 2013).* In any
518 case, substantial asynchronous release from the GC spine on yet longer time scales
519 (detected at up to 500 ms post TPU) was frequently observed, in line with earlier studies on
520 recurrent inhibition that localized the origin of asynchronous signalling within GCs (*Schoppa*
521 *et al. 1998; Chen et al. 2000; Isaacson 2001)*. This time course of asynchronous release also
522 matches with the duration of physiological postsynaptic GC spine Ca^{2+} transients *(Ona-Jodar*
523 *et al. 2020*). Thus, the microcircuit can operate across a wide range of latencies, which might
524 contribute to glomerulus-specific GC global AP firing latencies (*Kapoor & Urban 2006*), and
525 also can generate combined synchronous and asynchronous output.
526 *Na_v-mediated and NMDAR-mediated contributions to release*
527 How is postsynaptic Ca^{2+} entry coupled to release of GABA within the GC spine? Previously
528 we had shown via occlusion experiments that Ca^{2+} entry via NMDARs occurs independently

529 from Ca^{2+} entry mediated by the Na_v-HVACC pathway, since AMPAR-mediated
530 depolarization on its own is strong enough to lift the Mg^{2+} block, probably due to boosting by
531 the high GC spine neck resistance *(Bywalez et al. 2015)*. Therefore, we initially hypothesized
532 that the Na_v-HVACC pathway would provide the sole trigger for fast release of GABA, as in
533 classical release from axons (see also *Nunes & Kuner 2018*), validating the notion of the GC
534 spine as an independent mini-neuron that can generate output via its own local AP. Indeed,
535 blockade of either Na_v or HVACCs strongly reduced or abolished urIPSCs. However, in
536 subsequent experiments probing NMDAR contribution we observed that urIPSCs were also
537 massively reduced by blockade of NMDARs.
538 As a note of caution, activation of single GC spines via TPU might involve spurious activation
539 of extrasynaptic NMDARs. We had observed that TPU resulted in a slightly larger NMDA-
540 receptor mediated component of the postsynaptic Ca^{2+} signal than true synaptic activation
541 via glomerular stimulation (~ 65 % vs ~ 50% of $\Delta F/F$, *Bywalez et al. 2015; Egger et al. 2005*).
542 Thus, at least part of the strong impact of NMDARs observed here might have been rooted in
543 their over-activation. Therefore, we investigated recurrent inhibition elicited by single MC
544 APs, and could demonstrate that NMDAR blockade alone (which does not prevent GC spine
545 spike generation, *Bywalez et al. 2015*) also reduces recurrent inhibition. This effect was
546 found to be mutually occlusive with the effect of $GABA_AR$ blockade, arguing again in favor of
547 an essential role of NMDARs for GABA release and against systematic overstimulation in the
548 TPU experiments (see also Results, Methods).
549 Another interesting aspect of the strong influence of NMDARs on GC output is that this
550 property might serve to differentiate the MC↔GC microcircuit from the MC↔PV+ cell
551 microcircuit, since PV+ cells feature Ca^{2+}-permeable AMPARs and a probably absent
552 NMDAR component in response to MTC input (*Kato et al. 2013*). Thus, the urIPSC blockade
553 by APV observed here further argues in favor of a preferential activation of the MC↔GC
554 circuit by our experimental method.
555 In our earlier study of TPU-evoked Ca^{2+} signals in GC spines there was no obvious influence
556 of Na_v activation on NMDAR-mediated Ca^{2+} entry (*Bywalez et al. 2015*). At first, this finding
557 might seem at variance with the simulations in Fig. 5 that demonstrate a boosting of early
558 NMDAR-mediated Ca^{2+} currents by the spine spike. However, the simulations also indicate

559 that this extra contribution is not substantial in terms of added ΔF/F under our experimental
560 conditions and therefore could not be detected (Fig. 5D). In line with the fast NMDAR-
561 mediated Ca^{2+} spikelet, *Kampa et al. (2004*) have shown that the earlier the postsynaptic
562 membrane is depolarized after glutamate release, the more efficiently NMDARs will be
563 activated. These observations are of general importance in the context of spike-timing
564 dependent plasticity and electrical compartmentalization of spines (e.g. *Grunditz & Oertner*
565 *2004, Tonnesen & Nägerl 2016*).
566 How exactly do NMDARs now effect release? The Na_v/NMDAR-mediated Ca^{2+} spikelet
567 results in substantial and fast coincident activation of NMDARs and HVACCs, and our
568 ultrastructural evidence for presynaptic NMDARs implies that indeed these currents can feed
569 into the same presynaptic microdomain (see Results). This overlap bonus at the presynaptic
570 Ca^{2+} sensor (as predicted by the simulations) could thus explain the observed cooperative
571 signalling of HVACCs and NMDARs; further investigations are required to consolidate or
572 replace this hypothesis.
573 *Direct involvement of presynaptic NMDARs in GABA release*
574 Presynaptic actions of NMDARs at specific subsets of both glutamatergic and GABAergic
575 synapses have recently received attention (reviewed *in Bouvier et al. 2015; Banerjee &*
576 *Paulsen 2016*). Presynaptic NMDARs have been shown to play a role in plasticity induction
577 (e.g. *Duguid & Smart 2004*) or in modulation of basal synaptic transmission, where effects
578 are mostly observed upon repetitive transmitter release (e.g. *McGuiness et al. 2010*). In the
579 cerebellum, presynaptic NMDARs are also involved in enhancing spontaneous release of
580 GABA (*Glitsch & Marty 1999*), with similar observations for extrasynaptic NMDA receptors on
581 retinal A17 amacrine cells (V*eruki et al. 2019*). However, to our knowledge direct triggering of
582 release via presynaptic NMDARs during unitary transmission has not been observed so far,
583 adding another pathway to the already highly diverse signalling downstream of NMDARs.
584 The observed cooperation between Na_v/HVACCs and NMDARs relates our study back to the
585 initial studies on dendrodendritic recurrent inhibition (DDI), when it was concluded by several
586 groups that NMDARs can contribute directly to release from the reciprocal spine upon
587 extended release of glutamate from the MC dendrite (see Introduction), and *Schoppa et al.*
588 *(1998*) already speculated that this presynaptic function might be related to either Ca^{2+} entry

589 or depolarization. However, the relative contribution of NMDARs has been under debate and
590 it was demonstrated that under physiological conditions HVACC activation would be the
591 dominant release trigger (*Isaacson 2001*). While the standard DDI protocol, using 20-50 ms
592 long depolarizations, would evoke recurrent inhibition also in the presence of TTX (possibly
593 even enhanced, *Halabisky et al. 2000*), it was reported that recurrent inhibition in response to
594 shorter steps (< 5 ms) is substantially smaller than for the long step and reduced in TTX
595 (*Schoppa et al. 1998; Halabisky et al. 2000*). In view of our above results, the standard DDI
596 protocol is likely to recruit NMDAR-dependent pathways for triggering GABA release via
597 prolonged release of glutamate and subsequent summation of EPSPs in GC spines,
598 whereas short steps are more likely to trigger release via the GC spine spike. Thus, the
599 cooperation of NMDARs and HVACCs reconciles these earlier findings.

600 *Reciprocal inhibition and spontaneous inhibitory activity*

601 Spontaneous IPSCs are likely to predominantly originate from the more proximal lateral MC
602 dendrites (*Arnson & Strowbridge 2017*). The slightly larger mean amplitude of sIPSCs
603 compared to the triggered urIPSCs observed here might be explained by perisomatic
604 inhibitory contacts onto MCs, e.g. from type S GCs (*Naritsuka et al. 2009*). All three
605 antagonists of urIPSC generation (TTX, CTX, APV) were found to also substantially reduce
606 sIPSC frequency but not sIPSC amplitude. For Na_v blockade, strong effects on MC sIPSC
607 frequencies but not amplitude were reported also elsewhere (e.g. *Saghatelyan et al. 2005,*
608 *Arnson & Strowbridge 2017*) and are expected because of the blockade of both spontaneous
609 MC firing and the GC spine spike. The effect of HVACC blockade was less pronounced than
610 that of Na_vs, probably because spontaneous MC firing is less affected.

611 The substantial effect of NMDAR blockade on spontaneous IPSC frequencies was also
612 observed in other olfactory bulb studies (*Wellis & Kauer 1993; Schmidt & Strowbridge 2014;*
613 *but see Chen et al. 2000*). Several factors might contribute: (1) the long-lasting
614 depolarizations in MCs that are enhanced by NMDAR activation (*Carlson et al. 2000*), (2) the
615 presence of MC NMDA autoreceptors (*Sassoé-Pognetto et al. 2003*), and (3) the crucial role
616 of NMDARs for reciprocal release from the GC spine reported here, thus any spontaneous
617 release of glutamate from MCs is unlikely to trigger recurrent IPSCs in the presence of APV.

618

619 *Functional role of presynaptic NMDARs in GC spines: Linking coactive glomerular columns?*

620 While a presynaptic contribution of NMDARs to GABA release from GCs was already
621 demonstrated earlier (see above), our findings imply that not only **can NMDAR activation**
622 **trigger GABA release, it is actually necessary,** also in the presence of a Na_v-mediated
623 spine spike. This observation is very intriguing for several reasons, that we will briefly discuss
624 here:

625 (1) Role of granule cell APs for release from the reciprocal spine.

626 Notwithstanding the precise site of AP generation in GCs, any AP will propagate along
627 the GC dendrite and into the reciprocal spines perfectly well (*Egger et al. 2003, Pressler*
628 *& Strowbridge 2019*). The ensuing spine depolarization $V_m(t)_{SPINE}$ will resemble that of the
629 spine spike (see also *Aghvami et al. 2019*) which on its own, with NMDARs blocked,
630 according to our findings above cannot trigger GABA release. Therefore, any type of non-
631 local GC AP is rather unlikely to cause release of GABA by itself. This consequence
632 explains the lack of functional evidence for GC → MC transmission in coupled MC → GC
633 pairs, because APs elicited in the GC will not result in GABA release and thus no
634 inhibition will be exerted on the coupled MC (see Introduction).

635 It should be noted that extracellular stimulation of the GC layer can elicit MC inhibition,
636 even in the presence of APV (*e.g. Chen et al 2000, Egger et al. 2003, Arevian et al.*
637 *2008*). Possible explanations might be either that there is some small remaining
638 probability for GABA release from spiking GCs in the absence of glutamate, or that this
639 type of stimulation activates some as of yet unknown inhibitory input to MCs, e.g. via
640 deep short-axon cells or axons of EPL interneurons (*Nagayama et al. 2014, Burton*
641 *2017*).

642 (2) Role of GC-mediated lateral inhibition between MCs.

643 It is known by now that broad, far-range lateral inhibition between MCs within the EPL is
644 mediated by other interneurons than GCs (see Introduction). Thus, GCs are unlikely to
645 dominate bulbar lateral inhibition in terms of magnitude, i.e. total charge transfer, a view
646 that is also supported by other recent studies (*Fukunaga et al. 2014, Geramita & Urban*
647 *2017*). What then is the function of GC-mediated lateral inhibition?

648 As a consequence of the requirement of presynaptic NMDAR activation, we predict that
649 there will be no or at best very little GC-mediated lateral inhibition upon activation of a
650 single glomerular column, even if some columnar GCs fire APs or dendritic Ca^{2+} spikes
651 (which is fairly likely, *Mueller and Egger 2020*). We propose that GC-mediated **lateral**
652 **inhibition happens predominantly across coactive columns**. Thus the discovered
653 mechanism would allow GCs to perform lateral inhibition 'on demand', selectively on co-
654 active MCs, providing directed, dynamically switched lateral inhibition in a sensory
655 system with large numbers of receptor channels. GC-mediated lateral inhibition might
656 therefore participate in synthesizing the olfactory percept at the level of the bulb from the
657 individual olfactory receptor channels, most likely via MC synchronization in the gamma
658 band (e.g. *Laurent et al. 1996, Kashiwadani et al. 1999, Schoppa 2006, Brea et al 2009,*
659 *Li et al. 2015, Peace et al. 2017*), while at the same time preventing unnecessary energy
660 expenditure (i.e. if GABA release would happen from all reciprocal spines of an activated
661 GC). More importantly, inactive columns will remain sensitive for new stimuli or changing
662 components because they are not inhibited by active columns.
663 There is substantial prior evidence in the literature for both the activity-dependence and
664 NMDAR-dependence of GC-mediated lateral inhibition (*Arevian et al., 2008*). NMDAR
665 blockade is routinely used to dissect lateral inhibition in the glomerular layer from GC-
666 mediated lateral inhibition *(Shao et al. 2012, Najac et al. 2015, Geramita & Urban 2017)*.
667 Yet more importantly, in *in vivo* MC recordings there was a subset of MCs that responded
668 exclusively with inhibition to odor activation, mediated via glomerular layer neurons
669 (*Fukunaga et al., 2014, their Fig 4 and 7)*. Since there was no odor-evoked activity in
670 these MCs, our results imply that the presynaptic GC NMDARs could not be activated,
671 preventing GABA release from GCs.
672 As to behavioural evidence for our hypothesis, both GC NMDARs and Na_vs are known to
673 play a role specifically in discriminations between binary odorant mixtures in mice, since
674 in the same behavioral paradigm GC-specific knock-down (in about ~ 50% of GCs) of the
675 NMDAR-subunit GluN1 resulted in an increase in discrimination time of on average ~ 60
676 ms, and knock-down of Na_vs of ~ 85 ms versus control, while discriminations between
677 pure odors were not affected (*Abraham et al., 2010; Nunes & Kuner 2018*). These similar

effects are in line with our findings, since both modifications should prevent both recurrent and lateral inhibition. However, the relative impact of recurrent inhibition versus lateral inhibition is not known.

Conclusion: Hypothesis on the purpose of the reciprocal spine

In summary, our findings suggest that reciprocal spines allow the granule cell to selectively interact with coactive glomerular columns. Thus, the reciprocal spine might be a circuit motif that specifically enables efficient binding of dispersed olfactory representations, a coding task that this sensory modality needs to perform due to its large number of receptors. In other words, reciprocal spines with their unique synaptic arrangement and functionality, including spine spikes and presynaptic NMDARs, are likely to represent a special adaptation to the demands of sensory processing in the bulb. Of course, at this point this is a hypothesis that awaits further exploration via e.g. network simulations and in vivo approaches. Another intriguing yet more speculative potential function of target-activity-dependent output is that concurrent preactivation from glutamatergic cortical inputs onto reciprocal spines (ultrastructure in *Price & Powell 1970*) can also enhance lateral inhibition in addition to providing feed-forward inhibition, potentially allowing for a top-down projection of olfactory templates as has been proposed by *Zelano et al. (2011*).

696 **Methods**

697 *Animal handling, slice preparation and electrophysiology*

698 Animals used in our experiments were juvenile Wistar or VGAT-Venus transgenic rats
699 (VGAT-Venus /w-Tg(SLc32a1-YFP*)1Yyan) of either sex (P11 – P19). VGAT-Venus
700 transgenic rats are based on mouse BAC transgenic lines. They were generated by Drs. Y.
701 Yanagawa, M. Hirabayashi and Y. Kawaguchi at the National Institute for Physiological
702 Sciences, Okazaki, Japan, using pCS2-Venus provided by Dr. A. Miyawaki (*Uematsu et al.,*
703 *2008*), RRID: RGD_2314361. In this rat line, fluorescent Venus protein is preferentially
704 expressed in cells carrying the vesicular GABA transporter (VGAT), i.e. GABAergic neurons:
705 the localization of Venus-labeled cells across OB layers was found to be similar to that of
706 GABA-positive cells; direct colocalization in the cortex yielded an overlap of 97% (*Uematsu*
707 *et al., 2008*).

708 Sagittal olfactory bulb brain slices (thickness 300 µm) were prepared in ACSF (composition
709 see below) following procedures in accordance with the rules laid down by the EC Council
710 Directive (86/89/ECC) and German animal welfare legislation. Slices were incubated in a
711 water bath at 33°C for 30 min and then kept at room temperature (22°C) until recordings
712 were performed.

713 Olfactory bulb mitral cells were visualized by gradient contrast and recorded from in whole
714 cell voltage clamp mode (at -70 mV or +10 mV) or current clamp mode. Recordings were
715 made with an EPC-10 amplifier and Patchmaster v2.60 software (both HEKA Elektronik,
716 Lambrecht/Pfalz, Germany). Experiments were performed at room temperature (22°C).
717 Patch pipette resistance ranged from 5-6-MΩ. Mitral cells clamped at -70 mV were filled with
718 intracellular solution containing the following substances (in mM): (1) tip solution: 130 K-
719 Methylsulfate, 10 HEPES, 4 MgCl2, 2 Ascorbic acid, 10 Phosphocreatine-di-tris-salt, 2.5
720 Na2ATP, 0.4 NaGTP (2) backfilling solution: 110 Cs-Chloride, 10 HEPES, 10 TEA, 4MgCl2,
721 2 Ascorbic acid, 10 5-N-(2,6-dimethylphenylcarbamoylmethyl) triethylammonium bromide
722 (QX-314, Sigma), 0.2 EGTA, 10 Phosphocreatine, 2.5 Na2ATP, 0.4 NaGTP, 0.05 Alexa 594
723 (Ca^{2+} indicator, Thermofisher Scientific, Waltham. Massachusetts, US), at pH 7.3. Mitral cells
724 clamped at + 10 mV contained internal solution composed of: 125 Cs-methanesulfonate, 1

725 NaCl, 0.5 EGTA, 10 HEPES, 3 MgATP, 0.3 NaGTP, 10 Phosphocreatine-di-Tris-salt, 10 QX-
726 314, 0.05 Alexa 594, at pH 7.3.
727 For current clamp experiments in either MCs or GCs the internal solution contained: 130 K-
728 Methylsulfate, 10 HEPES, 4 MgCl2, 2 Ascorbic acid, 10 Phosphocreatine-di-Tris-salt, 2.5
729 Na2ATP, 0.4 NaGTP. Single APs were evoked by somatic current injection (3 ms, 1 nA) and
730 in MCs 5 APs were elicited for every recording condition. MCs with leak currents > 200 pA
731 and GCs with leak currents > 50 pA (at V_{hold} = - 70 mV) were discarded. For MCs, we chose
732 a hyperpolarized holding potential in order to reduce the activation of NMDA autoreceptors
733 on MC lateral dendrites.
734 The extracellular ACSF was bubbled with carbogen and contained (in mM): 125 NaCl, 26
735 $NaHCO_3$, 1.25 NaH_2PO_4, 20 glucose, 2.5 KCl, 1 $MgCl_2$, and 2 $CaCl_2$. The following
736 pharmacological agents were bath-applied in some experiments: bicucculline (BCC, 50 µM,
737 Sigma-Aldrich), ω-conotoxin MVIIC (CTX, 1 µM, Alomone, Jerusalem, Israel), TTX (500 nM,
738 Alomone), D-APV (25 µM, Tocris), gabazine (GBZ, 20 µM, Tocris). In pharmacological
739 experiments we waited for 10 minutes after wash-in of the drugs TTX, APV resp. CTX. In
740 CTX experiments 1mg/ml cyctochrome C was added to the ACSF. TTX voltage clamp
741 experiments were conducted at clamping potentials of -70 mV (n = 5 MCs) or + 10 mV (n = 7
742 MCs), whereas all CTX and APV voltage clamp experiments were conducted at + 10 mV.
743 *Combined two-photon imaging and uncaging*
744 Imaging and uncaging were performed on a Femto-2D-uncage microscope (Femtonics,
745 Budapest, Hungary). Two tunable, Verdi-pumped Ti:Sa lasers (Chameleon Ultra I and II
746 respectively, Coherent, Santa Clara, CA, USA) were used in parallel. The first laser was set
747 either to 900 nm for simultaneous excitation of YFP and Alexa 594 in one channel for
748 visualization of spines and the MC for urIPSC recordings (or the GC for uEPSP recordings),
749 and the second laser was set to 750 nm for uncaging of caged glutamate. The two laser lines
750 were directly coupled into the pathway of the microscope with a polarization cube (PBS102,
751 Thorlabs Inc, Newton, NJ, USA) and two motorized mirrors. As caged compound we used
752 DNI-caged glutamate (DNI; Femtonics). DNI was used in 1 mM concentration in a closed
753 perfusion circuit with a total volume of 12 ml. Caged compounds were washed in for at least
754 10 minutes before starting measurements. The uncaging laser was switched using an

755 electro-optical modulator (Pockels cell model 350-80, Conoptics, Danbury, CT, USA). The
756 emitted fluorescence was split into a red and a green channel with a dichroic mirror.

757 Triggering of mitral cell reciprocal IPSCs

758 The region of interest on a proximal lateral MC dendrite was moved to the center of the
759 scanning field. In some initial experiments, four uncaging spots were placed in close
760 apposition along the lateral MC dendrite in case of 'blind' uncaging (n = 8 out of total number
761 of successful experiments in n = 44 MCs). In most experiments, a single uncaging spot was
762 positioned near the region of interest, using YFP fluorescence of GABAergic cells in VGAT-
763 Venus rats as an optical guide to identify potential synaptic contacts between MC lateral
764 dendrites and GC spines.

765 The parameter settings for two-photon uncaging were as established previously on the same
766 experimental rig for precise mimicking of unitary synaptic Ca^{2+} transients in GC spines
767 (*Egger et al. 2005; Bywalez et al. 2015*). These parameter settings were routinely verified in
768 parallel test experiments, where we imaged Ca^{2+} transients in GC spines following TPU (as
769 in *Bywalez et al. 2015)*. The uncaging site was usually chosen within the top 10-30 µm below
770 the slice surface (since otherwise the visibility of spines in the Venus-VGAT rats was
771 compromised) and the uncaging power was adjusted to the depth of the uncaging site,
772 corresponding to a laser power of approximately 15 mW at the uncaging site (*Sobczyk et al.*
773 *2005*). The uncaging beam was positioned at ~ 0.2 - 0.5 µm distance from the MC
774 dendrite/GC spine head. The uncaging pulse duration was 1 ms. The scanning position was
775 readjusted if necessary before each measurement to account for drift. The microscope was
776 equipped with a 60x Nikon Fluor water immersion objective (NA 1.0; Nikon Instruments,
777 Tokyo, Japan). The microscope was controlled by MES v.5.3190 software (Femtonics). To
778 prevent overstimulation, the uncaging laser power was **not** increased if there was no
779 detectable response to the preset laser power (based on depth). While we cannot exclude
780 overstimulation per se, we would like to argue that systematic overstimulation is unlikely to
781 have occurred based on the following observations (see also Results):

782 - size of urIPSCs as compared to spontaneous activity (Fig. 1E)
783 - low reciprocal release probability from the spine (Fig. 1E)

784 - no extended asynchronous release compared to the classical experiments on
785 recurrent inhibition (mean total duration of TPU-evoked recurrent inhibition ~ 200 ms,
786 Fig. S1G, vs a mean half duration ~ 500 ms in e.g. *Schoppa et al. 1998, Isaacson*
787 *2001*)
788 - no evidence for toxicity in our stability experiments (Fig. 1F)
789 - main finding of dependency of recurrent inhibition on NMDAR activation confirmed by
790 method that does not involve uncaging

791 *Uncaging stability*

792 To test for the stability of uncaging evoked recurrent IPSCs in MCs, uncaging at a dendritic
793 region of interest was performed. If repeated uncaging led to the apparent occurrence of
794 urIPSCs within the same time window (see below for analysis details), the stability
795 measurement was continued by either uncaging 30 times in total with a frequency of 0.033
796 Hz (every 30 s) or 5 times in a row with 0.033 Hz followed by a 10 min break (to mimic the
797 time for wash-in of pharmacological compounds) and another round of uncaging (5x,
798 0.033Hz). urIPSC amplitudes were taken from averages of the first 5 – 10 and the last 5 – 10
799 uncaging sweeps and statistically compared with each other.

800 *Uncaging onto nearby GC spines*

801 For the control experiments where we tested whether adjacent GC spines could sense the
802 glutamate uncaged at an individual spine (Fig S1C, D, E), uncaging was performed as
803 described above and in (*Bywalez et al. 2015)* near a spine head of a GC filled with 100 µM
804 OGB-1 and 50 µM Alexa594 in whole-cell current clamp mode. Ca^{2+} imaging was perfomed
805 using a line scan through the spine head activated by TPU, the adjacent spine head and the
806 dendritic shaft in between.

807 *Electrophysiology: Data analysis and statistics*

808 Electrophysiological data were analysed with custom written macros in Igor pro
809 (Wavemetrics, Lake Oswego, OR, USA). Additional sIPSC and urIPSC analysis was
810 performed using the MiniAnalysis program (Synaptosoft, Decature, GA, USA) and Origin
811 (Northampton, MA, USA).

812 Detection of urISPCs Due to the high spontaneous activity, in order to test for the presence
813 of a signal we performed first an area and event analysis of IPSC traces (see below and Fig.
814 1D); if a signal was detected based on these analyses, we went on to search for individual
815 triggered urIPSCs by visual inspection of an overlay of the recorded traces. Individual IPSCs
816 were considered as uncaging-evoked when they repetitively occurred within the same time
817 window (width 3 ± 2 ms, n = 35 MCs) after uncaging and had similar kinetics (indicating a
818 similar location of the respective input on the MC dendrite). Signal types ranged from single
819 urIPSC events to barrages of urIPSCs lasting tens to hundreds of ms. The release probability
820 P_{r_GABA} was estimated based on 5 – 30 TPU samplings with a mean of 7.5 ± 1.7 stimulations
821 (n = 44 MCs).
822 Area analysis The area was measured in individual traces as the integrated activity above
823 baseline for a 500 ms pre-uncaging baseline window and for a 500 ms post-uncaging
824 window, in order to screen for the presence of a signal (Fig. 1D). The 500 ms extent of the
825 time windows was validated by our measurements of averaged barrage duration (see Fig.
826 S1G).
827 Delta (Δ) area values were calculated by subtracting the area of the 500 ms pre-uncaging
828 baseline window ('pre') from the 500 ms post-uncaging window ('post'), in order to isolate the
829 amount of uncaging-evoked inhibitory activity from spontaneous activity. If this procedure
830 was applied to averaged traces and the result was negative, the Δ_area value was set to
831 zero (i.e. no uncaging-evoked activity). While this procedure might still generate false
832 positives due to spontaneous bursts of activity in the post-uncaging window, it also prevents
833 a spurious cancelling of activity (false negative) that otherwise might happen upon averaging
834 Δ_area across an entire set of experiments. Δ_area values for pharmacological conditions
835 were normalized to control Δ_area in order to assess the net effect of drugs on uncaging-
836 evoked inhibitory activity (Fig. 2D, 3D, 4D).
837 Event analysis Within the individual recorded traces, the peak time points of individual IPSCs
838 were analysed. Peak search parameters in MiniAnalysis were adjusted in order to detect
839 potentially all IPSCs within a trace. For detailed spontaneous IPSC amplitude analysis,
840 IPSCs were sorted manually after the automated peak search and discarded if the amplitude
841 exceeded less than 5 pA and/or the IPSC onset was not be detected properly. Event counts

842 were averaged for the 500 ms pre-uncaging and the 500 ms post-uncaging windows,
843 respectively.
844 Evaluation of effects of pharmacological agents For determining drug effects, the averaged
845 urIPSC amplitudes were scaled down by the ratio of number of responses to total number of
846 trials, both in control and drug condition, in order to account also for changes in release
847 probability. If no single responses/urIPSCs could be detected anymore in the presence of
848 TTX, CTX or APV according to the criteria described above, we measured the mean
849 amplitude of V_m above baseline in the averaged response at the time point of the maximal
850 response amplitude in control condition. If this value was below 0, the response size was set
851 to 0 pA. If the value was larger than 0, we interpreted it as average drug response amplitude
852 including failures and thus did not scale it. This conservative method prevents false
853 negatives due to lacking sensitivity in individual trials in the presence of the drug.
854 Detection of spontaneous activity Spontaneous IPSCs were recorded prior to wash-in of DNI,
855 in the presence of DNI and in the presence of each pharmacological compound. For each
856 condition, data were analysed for a total duration of 20 s of recordings.
857 Analysis of afterhyperpolarizations All stable MC AP recordings within either baseline or drug
858 condition(s) were averaged (n = 5 recordings each). If between the conditions the holding
859 membrane potential changed by more than 0.3 mV, or the time course (onset of upstroke
860 relative to onset of step depolarization, width) and/or the amplitude of the AP changed by
861 more than 15% from their baseline values, the experiment was discarded. If single individual
862 recordings showed such variations, they were not included in the average. For each average,
863 the AHP amplitude was measured as the maximal negative deflection of the membrane
864 potential from the resting membrane potential.
865 *Simulations*
866 The simulations are based on a published compartmental model in NEURON (Aghvami et
867 al., 2019, ModelDB entry 244687). This model uses the 5-state gating model for NMDA
868 receptors (*Destexhe et al. 1998*), while the HVACC model is adopted from *Hemond et al.*
869 *2008,* with adjustments based on own Ca^{2+} current recordings (see *Aghvami et al. 2019*). For
870 the simulations shown in Fig. 5, there was no exogenous Ca^{2+} buffer included except for
871 panel D where fluorescence transients were simulated in the presence of 100 µM of the

872 Ca^{2+}-sensitive dye OGB-1 in order to emulate the experimental situation from *Bywalez et al.*
873 *2015*.
874 As a readout measure for the temporal overlap between I_{Ca_NMDAR} and I_{Ca_HVACC} we first
875 determined the FWHM (full width half maximum) for each current and then the interval within
876 which the two FWHMs overlapped. At this point, we focussed on temporal relationships and
877 did not account for current amplitudes or integrals, since Ca^{2+} concentration changes within
878 nanodomains cannot be properly simulated in NEURON and thus spine Ca^{2+} current
879 amplitudes are of limited meaning. We tested for the robustness of this measure
880 against variation of those model parameters that are crucially involved in the generation of
881 the spine spike, i.e. the resistance of the spine neck (R_{neck}), the conductance of AMPA
882 receptors (g_{AMPA}) and the voltage-gated sodium channel conductance (varied in proportion to
883 the potassium channel conductance, $g_{Na/K}$). Their nominal values in the GC model are 1.7
884 GΩ, 2000 pS and 0.5 S/cm^2 respectively. Each parameter was varied between up to 200% of
885 the nominal value, and down until no spine spike was generated any more.
886 *Immunogold labeling and electron microscopy*
887 Immunogold labeling was performed on cryosubstituted rat olfactory bulbs (n = 4 animals, 3
888 months old), that had been used previously; for further details on the fixation, embedding and
889 immunogold labeling procedure see (*Sassoè-Pognetto & Ottersen, 2000; Sassoè-Pognetto*
890 *et al., 2003*).
891 To maximize detection of the GluN1 subunit, we used a combination of two rabbit antisera as
892 described in *Sassoè-Pognetto et al. (2003)*. One antiserum (kindly donated by Anne
893 Stephenson) binds an extracellular domain (amino acid residues 17–35) common to all splice
894 variants of the GluN1 subunit (*Chazot et al. 1995; Racca et al. 2000*). The other antiserum
895 was raised against a C-terminal domain and recognizes four splice variants (Chemicon,
896 Temecula, CA; catalog No. AB1516).
897 For GluN2, we used a affinity-purified rabbit antibody raised against a synthetic peptide
898 corresponding to the C-terminus of the GluN2A subunit conjugated to BSA (Chemicon, cat.
899 no. AB1548). According to the manufacturer, this antibody recognizes the GluN2A and
900 GluN2B subunits in Western blot analysis of transfected cells.
901 *Ultrastructure data analysis and statistics*

902 Grid squares were analysed systematically for the presence of synaptic profiles (symmetric
903 and/or asymmetric) between GC spines and MC dendrites (Fig. 6; see also Fig. 1A in
904 *Sassoè-Pognetto & Ottersen 2000*). Synaptic profiles were then photographed at high
905 magnification (75.000 - 120.000x) with a side-mounted CCD camera (Mega View III,
906 Olympus Soft Imaging System). The plasma membrane of GC spines, when clearly visible,
907 was classified as either belonging to an asymmetric synaptic profile, a symmetric profile, or a
908 non-synaptic segment (see Fig. 6A2 for examples). The length of segments was measured
909 along the spine membrane curvature (using ImageJ 1.52 analysis software) and the number
910 of immunogold particles within a distance of ≤ 30 nm from the GC spine membrane was
911 counted for the individual segments. The lengths of non-synaptic segments were on average
912 longer than those of synaptic segments, which argues against an undersampling of gold
913 particle densities in non-synaptic membranes compared to synaptic membranes and thus a
914 false positive difference between the density distribution in non-synaptic membranes and
915 symmetric profiles (GluN1: mean non-synaptic segment length: 610 ± 400 nm, n = 138;
916 symmetric synaptic profiles: 270 ± 120 nm, n = 120; asymmetric synaptic profiles: 260 ± 110
917 nm, n = 111; similar results for GluN2, not shown). When both symmetric and asymmetric
918 synaptic profiles were visible in the same individual spine, the distance of such reciprocal
919 contacts was also measured along the curvature of the GC spine membrane.
920 The distribution of labeling along the axis perpendicular to the GC spine membrane (radial
921 axis) was determined by examining micrographs of transversely cut synaptic profiles, with
922 well defined presynaptic and postsynaptic membranes. Here all particles at distances up to
923 40 nm were counted to prevent a possible bias.
924 *Statistical tests*
925 All replicates were biological, i.e. physiological experiments were repeated in different cells
926 and ultrastructural analyses were conducted in different samples. Since sample sizes were
927 too small to test for the normal distribution of data and the main type of experiment was novel
928 (i.e. two-photon uncaging of glutamate on spines and detection of reciprocal IPSCs), all
929 electrophysiological data were analysed with non-parametric paired (*Wilcoxon matched*
930 pairs, e.g. for comparing data before and after washin of a drug) or unpaired (*Mann-Whitney-*
931 *U,* for comparing effects of different drugs) tests and expressed as mean ± SD. Based on the

932 properties of these tests and our long-term experience with non-parametric testing (since
933 *Egger et al. 2003*), we used a sample size of at least n = 7 for control type experiments (e.g,
934 stability of urIPSC recordings) and n = 10 for core experiments (effects of Na_v and NMDAR
935 blockade). For the main findings, effect sizes (Cohen's d) were calculated using G*Power
936 (3.1, https://www.psychologie.hhu.de/arbeitsgruppen/allgemeine-psychologie-und-
937 arbeitspsychologie/gpower.html). The density distributions of immunogold particles were
938 compared with the Kolmogorov-Smirnov test, which also does not make prior assumptions
939 on the nature of data distributions (https://www.wessa.net/rwasp_Reddy-Moores%20K-
940 S%20Test.wasp).
941
942 ***Author contributions***
943 VLR performed all uncaging experiments with MC recordings. LZ performed MC current
944 clamp recordings. MM performed supplementary MC recordings and granule cell uncaging
945 experiments. VLR, GB, MM, MSP and VE analyzed data. SSA performed simulations. VE
946 and VLR designed research and wrote the manuscript, with MSP contributing to the parts on
947 ultrastructure. BR provided DNI-caged glutamate and assisted in editing the manuscript.

948 ***Acknowledgments***
949 We thank Anne Pietryga-Krieger for expert technical assistance, Marius Stephan and Philipp
950 Seidel for assistance with IPSC analysis, Gagik Yeghiazaryan and Anna Bartalis for help with
951 MC current clamp recordings, Imre Vida for facilitating access to VGAT-Venus rats, Sigrun
952 Korsching and Yoshiyuki Kubota for advice on statistics and Ursula Koch for advice on
953 pharmacology and discussions on lateral inhibition. This work was funded mainly by the
954 German Federal Ministry for Education and Research (BMBF, 01GQ1104/01GQ1502), with
955 additional equipment funding by LMU-GSN, DFG-SFB 870 and funding for staff from GIF
956 (1479-418.13; all to VE), and by ERC 682426, GINOP_2.1.1-15-2016-00979, VKSZ_14-1-
957 2015-0155, 712821-NEURAM to BR.
958 ***Competing interests***
959 There are competing financial interests since BR is a founder of Femtonics Kft and a
960 member of its scientific advisory board. No other competing interests exist.
961

962 ***References***

963 1. Abraham, N. M., Egger, V., Shimshek, D. R., Renden, R., Fukunaga, I., Sprengel, R.,
964 Seeburg, P. H., Klugmann, M., Margrie, T. W., Schaefer, A. T., & Kuner, T. (2010). Synaptic
965 inhibition in the olfactory bulb accelerates odor discrimination in mice. *Neuron, 65*(3), 399-
966 411.
967 2. Aghvami, S., Müller, M., Araabi, B.N., & Egger V. (2019) Coincidence detection within the
968 excitable rat olfactory bulb granule cell spines. *J. Neurosci*. 39, 584-595. doi:
969 10.1523/JNEUROSCI.1798-18.2018
970 3. Angelo, K., & Margrie, T. W. (2011). Population diversity and function of hyperpolarization-
971 activated current in olfactory bulb mitral cells. *Sci Rep, 1*, 50. doi:10.1038/srep00050
972 4. Arevian A.,C., Kapoor, V., Urban, N.N. (2008). Activity-dependent gating of lateral inhibition
973 in the mouse olfactory bulb. *Nat Neurosci* 11, 80-87.
974 5. Arnson, H. A., & Strowbridge, B. (2017). Spatial Structure Of Synchronized Inhibition In The
975 Olfactory Bulb. *J Neurosci,* 37(43):10468 –10480. doi:10.1523/JNEUROSCI.1004-17.2017
976 6. Banerjee, A., Larsen, R.S., Philpot, B.D., & Paulsen,O. (2016). Roles of Presynaptic NMDA
977 Receptors in Neurotransmission and Plasticity. *Trends in Neurosciences* 39 (1).
978 http://dx.doi.org/10.1016/j.tins.2015.11.001
979 7. Bartel, D. L., Rela, L., Hsieh, L., & Greer, C. A. (2015). Dendrodendritic synapses in the
980 mouse olfactory bulb external plexiform layer. *J Comp Neurol, 523*(8), 1145-1161.
981 doi:10.1002/cne.23714
982 8. Bloodgood, B. L., & Sabatini, B. L. (2007). Ca(2+) signaling in dendritic spines. *Curr Opin*
983 *Neurobiol, 17*(3), 345-351. doi:10.1016/j.conb.2007.04.003
984 9. Bouvier, G., Bidoret, C., Casado, M., & Paoletti, P. (2015). Presynaptic NMDA receptors:
985 Roles and rules. *Neuroscience, 311*, 322-340. doi:10.1016/j.neuroscience.2015.10.033
986 10. Brea JN, Kay LM, Kopell NJ. (2009). Biophysical model for gamma rhythms in the olfactory
987 bulb via subthreshold oscilations. *Proc Natl Acad Sci U S A,* 106, 21954-9. doi:
988 10.1073/pnas.0910964106.
989 11. Burton SD. (2017). Inhibitory circuits of the main olfactory bulb. J Neurophysiol. 2017 Oct
990 1;118(4):2034-2051. doi: 10.1152/jn.00109.2017
991 12. Bywalez, W. G., Patirniche, D., Rupprecht, V., Stemmler, M., Herz, A. V. M., Pálfi, D., Rozsa,
992 B., & Egger, V. (2015). Local Postsynaptic Voltage-Gated Sodium Channel Activation in
993 Dendritic Spines of Olfactory Bulb Granule Cells. *Neuron, 85*(3), 590-601.
994 doi:10.1016/j.neuron.2014.12.051
995 13. Carlson, G. C., Shipley, M. T., & Keller, A. (2000). Long-lasting depolarizations in mitral cells
996 of the rat olfactory bulb. *J Neurosci, 20*(5), 2011-2021.
997 14. Chazot, P.L., Cik, M., & Stephenson, F.A. (1995). An investigation into the role of N-
998 glycosylation in the functional expression of a recombinant heteromeric NMDA receptor. Mol
999 Membr Biol, 12,331-337.
1000 15. Chen, W. R., Xiong, W., & Shepherd, G. M. (2000). Analysis of relations between NMDA

1001 receptors and GABA release at olfactory bulb reciprocal synapses. *Neuron, 25*(3), 625-633.
1002 16. Chiovini, B., Turi, G. F., Katona, G., Kaszas, A., Palfi, D., Maak, P., Szalay, G., Szabo, M. F.,
1003 Szabo, G., Szadai, Z., Kali, S., & Rozsa, B. (2014). Dendritic spikes induce ripples in
1004 parvalbumin interneurons during hippocampal sharp waves. *Neuron, 82*(4), 908-924.
1005 doi:10.1016/j.neuron.2014.04.004
1006 17. Crespo, C., Liberia, T., Blasco-Ibáñez, J.M., Nácher, J., & Varea, E. (2013). The circuits of
1007 the olfactory bulb. The exception as a rule. Anat Rec (Hoboken)., 296(9):1401-1412. doi:
1008 10.1002/ar.22732.
1009 18. Destexhe, A., Mainen, Z.F., & Sejnowski, T.J. (1998). Kinetic models of synaptic
1010 transmission. In: Methods in Neuronal Modeling (2nd edition; edited by Koch, C., & Segev,
1011 I.). MIT press, Cambridge, 1998, 1-25.
1012 19. Dietz SB, Markopoulos F, Murthy VN (2011). Postnatal development of dendrodendritic
1013 inhibition in the mammalian olfactory bulb. *Front Cell Neurosci* 5:10.
1014 20. Duguid, I., & Smart, T.G. (2004) Retograde activation of presynaptic NMDA receptors
1015 enhances GABA release at cerebellar interneuton-Purkinje cell synapses. *Nat Neurosci*, 7(5),
1016 525-533.
1017 21. Duménieu, M., Fourcaud-Trocmé, N., Garcia, S., & Kuczewski, N. (2015).
1018 Afterhyperpolarization (AHP) regulates the frequency and timing of action potentials in the
1019 mitral cells of the olfactory bulb: role of olfactory experience. Physiol Rep, 3(5). pii: e12344.
1020 doi: 10.14814/phy2.12344.
1021 22. Egger, V. (2008). Synaptic sodium spikes trigger long-lasting depolarizations and slow
1022 calcium entry in rat olfactory bulb granule cells. *Eur J Neurosci, 27*(8), 2066-2075.
1023 23. Egger, V., Svoboda, K., & Mainen, Z. F. (2003) Mechanisms of lateral inhibition in the
1024 olfactory bulb: efficiency and modulation of spike-evoked calcium influx into granule cells. J
1025 Neurosci 23:7551–7559.
1026 24. Egger, V., Svoboda, K., & Mainen, Z. F. (2005). Dendrodendritic synaptic signals in olfactory
1027 bulb granule cells: Local spine boost and global low-threshold spike. *J Neurosci, 25*, 3521-
1028 3530.
1029 25. Egger, V., & Urban, N. N. (2006). Dynamic connectivity in the mitral cell-granule cell
1030 microcircuit. *Semin Cell Dev Biol, 17*(4), 424-432.
1031 26. Friedman, D., & Strowbridge, B. W. (2000). Functional role of NMDA autoreceptors in
1032 olfactory mitral cells. *J Neurophysiol, 84*(1), 39-50. doi:10.1152/jn.2000.84.1.39
1033 27. Fukunaga, I., Herb, J. T., Kollo, M., Boyden, E. S., & Schaefer, A. T. (2014). Independent
1034 control of gamma and theta activity by distinct interneuron networks in the olfactory bulb. *Nat*
1035 *Neurosci, 17*(9), 1208-1216. doi:10.1038/nn.3760
1036 28. Geramita M, Urban NN. (2017) Differences in Glomerular-Layer-Mediated Feedforward
1037 Inhibition onto Mitral and Tufted Cells Lead to Distinct Modes of Intensity Coding. J Neurosci.
1038 2017 Feb 8;37(6):1428-1438.
1039 29. Glitsch, M., & Marty, A. (1999). Presynaptic Effects of NMDA in Cerebellar Purkinje Cells and

1040 Interneurons. J Neurosci, 19(2):511-519.
1041 30. Grunditz, Å., Holbro, N., Tian, L., Zuo, Y., & Oertner, T.G. (2008). Spine Neck Plasticity
1042 Controls Postsynaptic Calcium Signals through Electrical Compartmentalization. J Neurosci
1043 28:13457-13466.
1044 31. Halabisky, B., Friedman, D., Radojicic, M., & Strowbridge, B. W. (2000). Calcium influx
1045 through NMDA receptors directly evokes GABA release in olfactory bulb granule cells. *J*
1046 *Neurosci, 20*(13), 5124-5134.
1047 32. Hemond, P., Epstein, D., Boley, A., Migliore, M., Ascoli, G.A., & Jaffe, D.B. (2008). Distinct
1048 classes of pyramidal cells exhibit mutually exclusive firing patterns in hippocampal area
1049 CA3b. *Hippocampus* 18:411-424.
1050 33. Huang, L., Garcia, I., Jen, H.-I., & Arenkiel, B. R. (2013). Reciprocal connectivity between
1051 mitral cells and external plexiform layer interneurons in the mouse olfactory bulb. *Frontiers in*
1052 *Neural Circuits, 7*. doi:10.3389/fncir.2013.00032
1053 34. Isaacson, J. S. (1999). Glutamate spillover mediates excitatory transmission in the rat
1054 olfactory bulb. *Neuron, 23*(2), 377-384.
1055 35. Isaacson, J. S. (2001). Mechanisms governing dendritic gamma-aminobutyric acid (GABA)
1056 release in the rat olfactory bulb. *Proc Natl Acad Sci U S A, 98*(1), 337-342.
1057 36. Isaacson, J. S., & Strowbridge, B. W. (1998). Olfactory reciprocal synapses: dendritic
1058 signaling in the CNS. *Neuron, 20*(4), 749-761.
1059 37. Jackowski A, Parnavelas JG, Lieberman AR. (1978) The reciprocal synapse in the external
1060 plexiform layer of the mammalian olfactory bulb. Brain Res. 1978 Dec 22;159(1):17-28. doi:
1061 10.1016/0006-8993(78)90106-3.
1062 38. Kaeser, P. S., & Regehr, W. G. (2014). Molecular mechanisms for synchronous,
1063 asynchronous, and spontaneous neurotransmitter release. *Annu Rev Physiol, 76*, 333-363.
1064 doi:10.1146/annurev-physiol-021113-170338
1065 39. Kampa, B., Clements, J., Jonas, P., & Stuart, G.J. (2004) Kinetics of Mg2+ unblock of NMDA
1066 receptors: implications for spike-timing dependent synaptic plasticity. J Physiol, 556.2, 337-
1067 345.
1068 40. Kapoor, V., & Urban, N. N. (2006). Glomerulus-specific, long-latency activity in the olfactory
1069 bulb granule cell network. *J Neurosci, 26*, 11706-11719.
1070 41. Kashiwadani H, Sasaki YF, Uchida N, Mori K. (1999) Synchronized oscillatory discharges of
1071 mitral/tufted cells with different molecular receptive ranges in the rabbit olfactory bulb. J
1072 Neurophysiol. 82(4):1786-92.
1073 42. Kato, H. K., Gillet, S. N., Peters, A. J., Isaacson, J. S., & Komiyama, T. (2013). Parvalbumin-
1074 expressing interneurons linearly control olfactory bulb output. *Neuron, 80*(5),
1075 10.1016/j.neuron.2013.1008.1036. doi:10.1016/j.neuron.2013.08.036
1076 43. Kay, L. M. (2003). Two species of gamma oscillations in the olfactory bulb: dependence on
1077 behavioral state and synaptic interactions. *J Integr Neurosci, 2*(1), 31-44.
1078 44. Khawaled, R., Bruening-Wright, A., Adelman, J. P., & Maylie, J. (1999). Bicuculline Block of

1079 Small-conductance Calcium-activated Potassium Channels. *Pflügers Archiv : Eur J Physiol.*
1080 **438** (3): 314–321. doi:10.1007/s004240050915.
1081 45. Lagier, S., Carleton, A., & Lledo, P.-M. (2004). Interplay between Local GABAergic
1082 Interneurons and Relay Neurons Generates Gamma Oscillations in the Rat Olfactory Bulb. *J*
1083 *Neurosci*, 24(18):4382– 4392.
1084 46. Laurent G., Wehr M. & Davidowitz H. (1996) Temporal representations of odors in an
1085 olfactory network. *J. Neurosci.* **16**, 3837-3847 (1996)
1086 47. Lepousez, G., Csaba, Z., Bernard, V., Loudes, C., Videau, C., Lacombe, J., Epelbaum, J., &
1087 Viollet, C. (2010). Somatostatin interneurons delineate the inner part of the external plexiform
1088 layer in the mouse main olfactory bulb. *J Comp Neurol, 518*(11), 1976-1994.
1089 doi:10.1002/cne.22317
1090 48. Lester, R.A., Clements, J.D.,Westbrook, G.L., & Jahr, C.E. (1990) NMDAR Channel kinetics
1091 determine the time course of NMDA receptor-mediated synaptic currents. Nature,
1092 346(6284):565-567.
1093 49. Li A., Gire H.G., & Restrepo D. (2015) Spike-Field Coherence in a Population of Olfactory
1094 Bulb Neurons Differentiates between Odors Irrespective of Associated Outcome. J Neurosci
1095 35(14):5808-5822
1096 50. Matsuno T, Kiyokage E, Toida K. (2017) Synaptic distribution of individually labeled mitral
1097 cells in the external plexiform layer of the mouse olfactory bulb. J Comp Neurol. 525(7):1633-
1098 1648. doi: 10.1002/cne.24148.
1099 51. McGuinness, L., Taylor, C., Taylor, R.D., Yau, C., Langenhan, T., Hart, M.L., Christian, H.,
1100 Tynan, P.W., Donnelly, P., & Emptage, N.J. (2010). Presynaptic NMDARs in the
1101 hippocampus facilitate transmitter release at theta frequency. *Neuron*, 68(6):1109-1127. doi:
1102 10.1016/j.neuron.2010.11.023.
1103 52. McIntyre, A. B. R., & Cleland, T. A. (2016). Biophysical constraints on lateral inhibition in the
1104 olfactory bulb. *Journal of Neurophysiology, 115*(6), 2937-2949. doi:10.1152/jn.00671.2015
1105 53. McTavish TS, Migliore M, Shepherd GM, Hines ML. (2012) Mitral cell spike synchroniy
1106 modulated by dendrodendritic synapse location. Front Comput Neurosci. 6:3. doi:
1107 10.3389/fncom.2012.00003.
1108 54. Miller, J. P., Rall, W., & Rinzel, J. (1985). Synaptic amplification by active membrane in
1109 dendritic spines. *Brain Res, 325*(1-2), 325-330.
1110 55. Miyamichi, K., Shlomai-Fuchs, Y., Shu, M., Weissbourd, B. C., Luo, L., & Mizrahi, A. (2013).
1111 Dissecting Local Circuits: Parvalbumin Interneurons Underlie Broad Feedback Control of
1112 Olfactory Bulb Output. *Neuron, 80*(5), 1232-1245. doi:10.1016/j.neuron.2013.08.027
1113 56. Mori, K., Nagao, H., & Yoshihara, Y. (1999). The olfactory bulb: Coding and Processing of
1114 odor molecule information. *Science*, 286, 711-715.
1115 57. Mueller M**.,** Egger V. (2020) Dendritic integration in olfactory bulb granule cells: Threshold for
1116 lateral inhibition and role of active conductances upon simultaneous activation.
1117 *PLOS Biology*. doi.org/10.1371/journal.pbio.3000873

1118 58. Nagayama S, Homma R, Imamura F. (2014) Neuronal organization of olfactory bulb circuits.
1119 Front Neural Circuits. 8:98. doi: 10.3389/fncir.2014.00098.
1120 59. Najac M, Sanz Diez A, Kumar A, Benito N, Charpak S, De Saint Jan D. (2015)
1121 Intraglomerular lateral inhibition promotes spike timing variability in principal neurons of the
1122 olfactory bulb. J Neurosci. 35(10):4319-31. doi: 10.1523/JNEUROSCI.2181-14.2015.
1123 60. Naritsuka, H., Sakai, K., Hashikawa, T., Mori, K., & Yamaguchi, M. (2009). Perisomatic-
1124 targeting Granule Cells in the Mouse Olfactory Bulb. *J Comp Neurol*, 525, 409-426.
1125 61. Nunes, D., & Kuner, T. (2018). Axonal sodium channel NaV1.2 drives granule cell dendritic
1126 GABA release and rapid odor discrimination. *PLoS Biol, 16*(8), e2003816.
1127 doi:10.1371/journal.pbio.2003816
1128 62. Ona Jodar T., Lage-Rupprecht V., Abraham N.M., Rose C.R. & Egger V. (2020).
1129 Local postsynaptic signalling on slow time scales in reciprocal olfactory bulb granule
1130 cell spines matches asynchronous release. bioRxiv 2020.09.03.281642 doi:
1131 https://doi.org/10.1101/2020.09.03.281642
1132 63. Pálfi, D., Chiovini, B., Szalay, G., Kaszás, A., Turi, G.F., Katona, G., Ábrányi-Balogh, P.,
1133 Szőri, M., Potor, A., Frigyesi, O., Lukácsné Haveland, C., Szadai, Z., Madarász, M.,
1134 Vasanits-Zsigrai, A., Molnár-Perl, I., Viskolcz, B., Csizmadia, I.G., Mucsi, Z., & Rózsa, B.
1135 (2018). High efficiency two-photon uncaging coupled by the correction of spontaneous
1136 hydrolysis. Org Biomol Chem. 16(11):1958-1970. doi: 10.1039/c8ob00025e.
1137 64. Peace ST, Johnson BC, Li G, Kaiser ME, Fukunaga I, Schaefer AT, Molnar AC, Cleland TA
1138 (2017) Coherent olfactory bulb gamma oscillations arise from coupling independent columnar
1139 oscillations. bioRxiv 213827; doi: https://doi.org/10.1101/213827
1140 65. Pressler, R. T., & Strowbridge, B. W. (2017). Direct Recording of Dendrodendritic Excitation
1141 in the Olfactory Bulb: Divergent Properties of Local and External Glutamatergic Inputs
1142 Govern Synaptic Integration in Granule Cells. *J Neurosci, 37*(49), 11774-11788.
1143 doi:10.1523/JNEUROSCI.2033-17.2017
1144 66. Pressler, R. T., & Strowbridge, B. W. (2019). Functional specialization of interneuron
1145 dendrites: Identification of action potential initiation zone in axonless olfactory bulb granule
1146 cells. J Neurosci. 39(49):9674-9688. doi: 10.1523/JNEUROSCI.1763-19.2019
1147 67. Price J.L. & Powell T.P. (1970) An experimental study of the origin and the course of the
1148 centrifugal fibres to the olfactory bulb in the rat. *J Anat.* **107**:215-237
1149 68. Racca, C., Stephenson, F.A., Streit, P., Roberts, J.D., & Somogyi, P. (2000). NMDA receptor
1150 content of synapses in stratum radiatum of the hippocampal CA1 area. *J Neurosci.*
1151 20(7):2512-2522.
1152 69. Rannals, M. D., & Kapur, J. (2011). Homeostatic strengthening of inhibitory synapses is
1153 mediated by the accumulation of GABA(A) receptors. *J Neurosci, 31*(48), 17701-17712.
1154 doi:10.1523/JNEUROSCI.4476-11.2011
1155 70. Saghatelyan, A., Roux, P., Migliore, M., Rochefort, C., Dasmaisons, D., Charneau, P.,
1156 Shepherd, G.M. & Lledo, P.-M. (2005). Activity-dependent adjustments of the inhibitory

network in the olfactory bulb following early postnatal deprivation. *Neuron 46*, 103-116Sailor, K.A., Valley, M. T., Wiechert, M. T., Riecke, H., Sun, G. J., Adams, W., . . . Lledo, P.-M. (2016). Persistent Structural Plasticity Optimizes Sensory Information Processing in the Olfactory Bulb. *Neuron, 91*(2), 384-396. doi:http://dx.doi.org/10.1016/j.neuron.2016.06.004

71. Sassoé-Pognetto, M., & Ottersen, O. P. (2000). Organization of Ionotropic Glutamate Receptors at Dendrodendritic Synapses in the Rat Olfactory Bulb. *J Neurosci*, 20(6):2192–2201.
72. Sassoé-Pognetto, M., Utvik, J. K., Camoletto, P., Watanabe, M., Stephenson, F. A., Bredt, D. S., & Ottersen, O. P. (2003). Organization of postsynaptic density proteins and glutamate receptors in axodendritic and dendrodendritic synapses of the rat olfactory bulb. *J Comp Neurol, 463*(3), 237-248.
73. Schmidt, L. J., & Strowbridge, B. W. (2014). Modulation of olfactory bulb network activity by serotonin: synchronous inhibition of mitral cells mediated by spatially localized GABAergic microcircuits. *Learn Mem, 21*(8), 406-416. doi:10.1101/lm.035659.114
74. Schoppa, N. E., Kinzie, J. M., Sahara, Y., Segerson, T. P., & Westbrook, G. L. (1998). Dendrodendritic inhibition in the olfactory bulb is driven by NMDA receptors. *J Neurosci, 18*(17), 6790-6802.
75. Schoppa NE (2006) AMPA/kainate receptors drive rapid output and precise synchrony in olfactory bulb granule cells. J Neurosci 26:12996-13006.
76. Shao Z, Puche AC, Liu S, Shipley MT. (2012) Intraglomerular inhibition shapes the strength and temporal structure of glomerular output. J Neurophysiol. 108(3):782-93. doi: 10.1152/jn.00119.2012.
77. Sobczyk, A., Scheuss, V., & Svoboda, K. (2005). NMDA receptor subunit-dependent [Ca2+] signaling in individual hippocampal dendritic spines. *J Neurosci, 25*(26), 6037-6046. doi:10.1523/JNEUROSCI.1221-05.2005
78. Spruston, N. (2008). Pyramidal neurons: dendritic structure and synaptic integration. *Nat Rev Neurosci, 9*(3), 206-221. doi:10.1038/nrn2286
79. Stanley, E. F. (2016) The Nanophysiology of Fast Transmitter Release. *Trends Neurosci*. 39 (3). http://dx.doi.org/10.1016/j.tins.2016.01.005
80. Toida, K., Kosaka, K., Heizmann, C. W., & Kosaka, T. (1994). Synaptic contacts between mitral/tufted cells and GABAergic neurons containing calcium-binding protein parvalbumin in the rat olfactory bulb, with special reference to reciprocal synapses between them. *Brain Res, 650*(2), 347-352.
81. Tonnesen, J., & Nagerl, U. V. (2016) Dendritic Spines as Tunable Regulators of Synaptic Signals. *Front Psychiatry* 7:101. doi: 10.3389/fpsyt.2016.00101
82. Uematsu, M., Hirai, Y., Karube, F., Ebihara, S., Kato, M., Abe, K., . . . Kawaguchi, Y. (2008). Quantitative Chemical Composition of Cortical GABAergic Neurons Revealed in Transgenic Venus-Expressing Rats. *Cerebral Cortex, 18*(2), 315-330. doi:10.1093/cercor/bhm056
83. Veruki, M. L., Zhou, Y., Castilho, A., Morgans, C. W., & Hartveit, E. (2019) Extrasynaptic

1196 NMDA Receptors on Rod Pathway Amacrine Cells: Molecular Composition, Activation, and
1197 Signaling. *J Neurosci* 39: 627-650. Doi: 10.1523/JNEUROSCI.2267-18.2018
1198 84. Wellis, D. P., & Kauer, J. S. (1993). GABAA and glutamate receptor involvement in
1199 dendrodendritic synaptic interactions from salamander olfactory bulb. *J Physiol, 469*, 315-
1200 339.
1201 85. Woolf, T. B., Shepherd, G. M., & Greer, C. A. (1991). Serial reconstructions of granule cell
1202 spines in the mammalian olfactory bulb. *Synapse, 7*(3), 181-192.
1203 86. Zelano C, Mohanty A, Gottfried JA. (2011) Olfactory predictive codes and stimulus templates
1204 in piriform cortex. Neuron. 72(1):178-87. doi: 10.1016/j.neuron.2011.08.010.